

An empirical model of the occurrence rate of low latitude post-sunset plasma irregularities derived from CHAMP and Swarm magnetic observations

Claudia Stolle¹, Tarique Adnan Siddiqui², Lucas Fabian Schreiter³, Suman K. Das¹, Ina Rusch¹, and Martin Rother⁴

¹Leibniz Institut of Atmospheric Physics at the University of Rostock

²Leibniz Institute of Atmospheric Physics

³GFZ German Research Centre for Geosciences

⁴Deutsches GeoForschungsZentrum, GFZ

December 1, 2023

Abstract

The prediction of post-sunset equatorial plasma depletions (EPDs), often called ionospheric plasma bubbles, has remained a challenge for decades. In this study, we introduce the Ionospheric Bubble Probability (IBP), an empirical model predicting the occurrence probability of EPDs derived from 9 years of CHAMP and 8.5 years of Swarm magnetic field measurements. The model predicts the occurrence probability of EPDs for a given longitude, day of year, local time and solar activity, for the altitude range 350-500 km, and low geographic latitudes of $\pm 45^\circ$. IBP has been found to successfully reconstruct the distribution of EPDs as reported in previous studies from independent data. IBP has been further evaluated using one-year of partly untrained data of the Ionospheric Bubble Index (IBI). IBI is a Level 2 product of the Swarm satellite mission used for EPD identification. The relative operating characteristics (ROC) curve shows positive excursion above the no-skill line with Hanssen and Kuiper's Discriminant (H&KSS) score of 0.66, 0.73, and 0.65 at threshold model outputs of 0.22, 0.18, and 0.18 for Swarm A, B, and C satellites, respectively. Additionally, the reliability plots show proximity to the diagonal line with a fairly decent Brier Skill Score (BSS) of 0.317, 0.320, and 0.316 for Swarm A, B, and C respectively. These tests indicate that the model performs significantly better than a no-skill forecast. The IBP model offers a compelling glimpse into the future of EPD forecasting, thus demonstrating its potential to reliably predict EPD occurrences. The IBP model is made publicly available.

1 **An empirical model of the occurrence rate of low**
2 **latitude post-sunset plasma irregularities derived from**
3 **CHAMP and Swarm magnetic observations**

4 **C. Stolle¹, T. A. Siddiqui¹, L. Schreiter^{2,3}, S. K. Das¹, I. Rusch¹, M. Rother³**

5 ¹Leibniz Institute of Atmospheric Physics at the University of Rostock, Kühlungsborn, Germany

6 ²Institute of Geodesy, Technical University of Berlin, Germany

7 ³GFZ German Research Centre for Geosciences, Helmholtz Centre Potsdam, Germany

8 **Key Points:**

- 9 • The IBP model to estimate the occurrence probability of post-sunset equatorial
10 plasma depletions (EPDs) is introduced.
11 • IBP shows high performance in predicting EPD occurrence for longitude, local time,
12 day of year, solar activity, at altitudes of 350-500 km.
13 • The IBP model is publicly available including documentation.

Corresponding author: Claudia Stolle, cstolle@iap-kborn.de

Abstract

The prediction of post-sunset equatorial plasma depletions (EPDs), often called ionospheric plasma bubbles, has remained a challenge for decades. In this study, we introduce the Ionospheric Bubble Probability (IBP), an empirical model to predict the occurrence probability of EPDs derived from 9 years of CHAMP and 8.5 years of Swarm magnetic field measurements. The model predicts the occurrence probability of EPDs for a given longitude, day of year, local time and solar activity, for the altitude range 350-500 km, and low geographic latitudes of $\pm 45^\circ$. IBP has been found to successfully reconstruct the distribution of EPDs as reported in previous studies from independent data. IBP has been further evaluated using one-year of partly untrained data of the Ionospheric Bubble Index (IBI). IBI is a Level 2 product of the Swarm satellite mission used for EPD identification. The relative operating characteristics (ROC) curve shows positive excursion above the no-skill line with Hanssen and Kuiper's Discriminant (H&KSS) score of 0.66, 0.73, and 0.65 at threshold model outputs of 0.22, 0.18, and 0.18 for Swarm A, B, and C satellites, respectively. Additionally, the reliability plots show proximity to the diagonal line with a fairly decent Brier Skill Score (BSS) of 0.317, 0.320, and 0.316 for Swarm A, B, and C respectively. These tests indicate that the model performs significantly better than a no-skill forecast. The IBP model offers a compelling glimpse into the future of EPD forecasting, thus demonstrating its potential to reliably predict EPD occurrences. The IBP model is made publicly available.

Plain Language Summary

[Post-sunset equatorial plasma depletions (EPDs), often called ionospheric plasma bubbles, are a severe threat for reliable radio wave communication. However, their predictability has remained a challenge for the scientific community for decades. In this study, we introduce the Ionospheric Bubble Probability (IBP) model predicting the occurrence probability of post-sunset EPDs for a given longitude, day of year, local time and solar activity, for the altitude range 350-500 km, and low geographic latitudes of $\pm 45^\circ$. To this aim we have used 9 years of CHAMP and 8.5 years of Swarm magnetic field measurements. The IBP model predictions have been found to agree well with climatologies derived from independent data and performs largely better than unskilled forecasts. The IBP model is made publicly available.]

1 Introduction

The post-sunset equatorial and low-latitude ionosphere is susceptible to irregularities associated with F region plasma instability, popularly known as equatorial plasma depletions (EPDs) or ionospheric plasma bubbles. EPDs are regions of steep plasma depletions of several orders of magnitude in electron density with scale sizes ranging from thousands of kilometers down to meters (e.g., D. L. Hysell & Seyler, 1998; Lühr et al., 2014; Su et al., 2001). EPD is believed to be governed by the Rayleigh-Taylor (RT) instability mechanism which operates at the bottomside F region when uplifted during evening time post-sunset rise driven by the pre-reversal enhancement (PRE) of zonal electric field over the dip equator (e.g., Balsley et al., 1972; Haerendel, 1973; Ossakow, 1981; Sultan, 1996; Woodman & La Hoz, 1976; Tsunoda, 2005). The growth of RT instability depends on various ionospheric and thermospheric parameters which include F layer height, zonal (eastward) electric field, bottomside density gradient, meridional wind and perturbation in electron density in the form of seed (e.g., Kelley, 2009). EPDs have been found to exhibit serious threats to radio waves employed for satellite-based communication/navigation applications by producing random fluctuations in signal amplitude and phase known as scintillations. Based on simultaneous observations of plasma density and Global Positioning System (GPS) observables on board the Swarm satellite mission, Xiong et al. (2016, 2020) showed the positive relation between the strengths of EPDs and the severeness of

64 GPS scintillations to even total signal losses. Therefore, predicting EPD occurrence is
65 of absolute necessity.

66 Although the underlying principle of RT instability is well understood (e.g., Kel-
67 ley, 2009; Sultan, 1996), understanding the variability in EPD occurrence on a day-to-
68 day basis continues to be puzzling (e.g., Abdu, 2019; Basu et al., 2009; Carter et al., 2014;
69 Chou et al., 2020; Manju & Aswathy, 2020; Rajesh et al., 2017; Retterer & Roddy, 2014;
70 Saito & Maruyama, 2007; Shinagawa et al., 2018; Tsunoda et al., 2010, 2018; Yamamoto
71 et al., 2018; Das et al., 2021; D. L. Hysell et al., 2022; Patra & Das, 2023). While the
72 PRE has been found to show a remarkable agreement with EPD occurrence climatolog-
73 ically (e.g., Clemesha & Wright, 1966; Dabas et al., 2003; Fejer et al., 1999; Gentile et
74 al., 2006b; D. Hysell & Burcham, 2002; Stolle et al., 2008; Su et al., 2008; Tsunoda, 2005;
75 Huang & Hairston, 2015), it fails to account on its day-to-day occurrence variability (e.g.,
76 Abdu et al., 1983; Fukao et al., 2006; Saito & Maruyama, 2006, 2007). Intriguingly, the
77 growth rate of RT instability has been found to display similar uncertainty (e.g., Shi-
78 nagawa et al., 2018; Das et al., 2021; Aa et al., 2023). Since the EPD occurrence shows
79 a large variability both in small- and large-longitudinal scales (e.g., Kil et al., 2009; Kil
80 & Heelis, 1998a; Martinis et al., 2021; Singh et al., 1997; Stolle et al., 2008; Tsunoda et
81 al., 2018; Tsunoda & White, 1981), predicting EPD occurrence becomes even more chal-
82 lenging. Now, it is fairly well understood that missing understanding of the spatio-temporal
83 behaviour of EPDs, i.e. growth, zonal movement and decay of EPDs, along with the paucity
84 of continuous measurements of ionospheric parameters is the cause for the challenge in
85 predicting the day-to-day occurrence variability of EPDs (e.g., Das et al., 2021; Li et al.,
86 2021; D. L. Hysell et al., 2021; Patra & Das, 2023).

87 While for a long time, traditional methods such as in situ density measurements,
88 optical imagers and radio wave sounding have been employed to study the day-to-day,
89 global, and climatological occurrence of EPDs (e.g., Woodman & La Hoz, 1976; Farley
90 et al., 1970; Kudeki & Bhattacharyya, 1999; Sahai et al., 1994, 2000; Kil & Heelis, 1998b;
91 Fagundes et al., 1999; Burke et al., 2004; Gentile et al., 2011; Huang et al., 2014; Mar-
92 tinis & Mendillo, 2007; Das et al., 2021; Aa et al., 2023), subsequently, it has been found
93 that magnetic field perturbations associated with the diamagnetic current linked to steep
94 density gradient at the edges of the EPDs can also be used for characterizing EPDs (e.g.,
95 Lühr et al., 2002; Rodríguez-Zuluaga et al., 2019). Diagnosing EPDs through those sig-
96 natures in the magnetic field and electron density, Stolle et al. (2006) could successfully
97 reconstruct the well-known EPB climatology using Flux-Gate Magnetometer (FGM) mea-
98 surements on-board the Challenging Mini-Satellite Payload (CHAMP) which similarly
99 were obtained by traditional methods based on plasma density data from other satel-
100 lite missions (e.g., Gentile et al., 2006b; Xiong et al., 2010). This success led to the in-
101 troduction of the Ionospheric Bubble Index (IBI) as a standard Level 2 (L2) data prod-
102 uct of the Swarm mission for the detection of EPDs (e.g., Park et al., 2013). Recently,
103 Reddy et al. (2023) have utilized a machine learning (ML) based AI Prediction of EPBs
104 (APE) model to predict the IBI. Their model is derived from 8 years of Swarm data. Fea-
105 ture analyses revealed that F10.7 is the most important feature in driving the EPB pre-
106 dictions, whereas latitude is the least.

107 The advantage of EPD climatology derived from in situ observations of polar-orbiting,
108 Low Earth Orbit (LEO) satellites is their global coverage. However, it should be noted
109 that these satellites can only detect those irregularities that have evolved into plumes
110 reaching F region altitudes at or above the F2 peak. Conversely, the bottom-side F re-
111 gion irregularities, from which plumes may evolve, occur more frequently than F region
112 plumes are observed, e.g., almost every evening throughout the year and solar cycle, e.g.,
113 in the American sector. A comprehensive investigation of the irregularity occurrence de-
114 rived from 20 years of incoherent scatter radar data at the Jicamarca radio observatory
115 has been provided by Zhan et al. (2018). Accordingly, based on 10 years of ground-based
116 GPS observations distributed in South America, Macho et al. (2022) indicated some ac-

117 tivity of weak scintillations also during low solar flux years, while moderate or intense
 118 scintillations did only occur during moderate or high solar flux years.

119 This article introduces an empirical model of the occurrence probability of post-
 120 sunset F region EPDs called the Ionospheric Bubble Probability (IBP) model. The IBP
 121 is derived from the detection of magnetic field perturbations associated with EPDs ob-
 122 tained from 9 years of CHAMP and 8.5 years of Swarm observations in the geomagnetic
 123 field. The model predicts the EPD occurrence rate for a given longitude, day of year,
 124 local time and solar activity, for the altitude range 350-500 km, and low geographic lat-
 125 itudes of $\pm 45^\circ$. The occurrence probability is given in the range of 0 to 1, from a 0%
 126 to 100% probability, respectively. The structure of this manuscript goes as following. Sec-
 127 tion 2 provides a description of the data on which the model is based, section 3 describes
 128 the model development methods, section 4 shows the model results, section 5 provides
 129 model validation and discussion, and finally, conclusions are described in section 7. The
 130 forward model code is available from URL: <https://igit.iap-kborn.de/ibp/ibp-model>.

131 2 Data

132 2.1 Swarm satellite mission

133 The Swarm satellite mission is a constellation consisting of three identical satel-
 134 lites Alpha, Bravo and Charlie (A, B and C) launched in November 2013 into near-circular
 135 orbits at an altitude of approximately 490 km (Friis-Christensen et al., 2006; Olsen et
 136 al., 2013). Following orbital maneuvers in April 2014, Swarm A and C fly in a side-by-
 137 side configuration with an inclination of 87.4° and an initial altitude of about 460 km
 138 (see Figure 1), while Swarm B flies at an inclination of 88° and at a higher orbit of ini-
 139 tially about 530 km altitude. Swarm B has been precessing away from the lower pair at
 140 a rate of approximately 1.5 h of local time per year while Swarm A and C precess west-
 141 ward in local time at a rate of 2.7 h per month (Knudsen et al., 2017). The Swarm satel-
 142 lites cover all local times about every 4 months. The satellites carry, among other instru-
 143 ments, a magnetometer package consisting of an Absolute Scalar Magnetometer (ASM)
 144 and a Vector Field Magnetometer (VSM), which provides precise measurements of the
 145 Earth’s magnetic field at the satellite location at 1 Hz frequency. Each satellite also car-
 146 ries a spherical Langmuir probe as part of the Electric Field Instrument (EFI) provid-
 147 ing plasma density observations at 2 Hz frequency (Knudsen et al., 2017).

148 It is known that EPDs can be detected by high-precision magnetometers on board
 149 low earth orbit (LEO) satellites from their diamagnetic effects as regions of locally de-
 150 pleted plasma are characterized by enhanced magnetic field strength (e.g., Lühr et al.,
 151 2003; Stolle et al., 2006; Park et al., 2013). For the Swarm mission, the European Space
 152 Agency (ESA) has introduced the Ionospheric Bubble Index (IBI) as a standard Level 2 (L2)
 153 data product, which is generated from in situ magnetic field and plasma observations
 154 onboard the Swarm satellites and provides detections of EPDs along Swarm orbits. The
 155 IBI product considers not only the characteristic small-scale variations in the magnetic
 156 field to detect EPDs but also the concurrent change in plasma density to confirm these
 157 detected EPDs. The detection threshold of EPDs based on their diamagnetic effects is
 158 set to 0.15 nT. If the correlation between the magnetic field and electron density is suf-
 159 ficiently high (i.e. $p^2 > 0.5$, where p is the pearson correlation coefficient), which confirms
 160 the diamagnetic effect, the magnetic fluctuation is flagged as confirmed EPD. The IBI
 161 product provides a binary indicator for each of the low latitude (below 45°), night side
 162 (18-06LT), 1 Hz magnetic readings whether the measurement is affected by an EPD or
 163 not. If the data quality does not allow for EPD detection, e.g., due to enhanced noise
 164 or too many data gaps, the data is flagged by an integer value larger than 1. The de-
 165 tailed description of the IBI product and of its derivation is outlined in Park et al. (2013).
 166 Swarm data between 01 January 2014 and 31 December 2022 have been used in this study

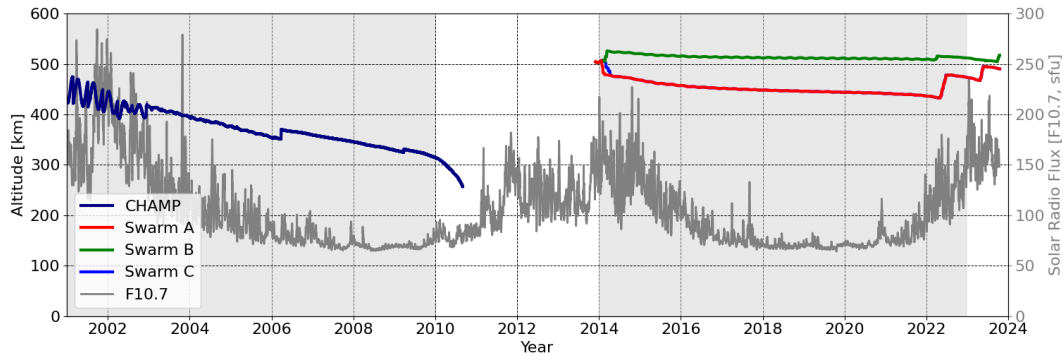


Figure 1. Orbit altitude evolution of the CHAMP and Swarm satellites. The grey line indicates daily values of the F10.7 solar activity index. The light grey areas indicate the times of satellite data which were selected to derive the IBP model.

167 to derive the model. The mean satellite altitudes were around 480 km for Swarm A and
 168 C and 510 km for Swarm B (see Figure 1).

169 2.2 CHAMP satellite mission

170 CHAMP (CHallenging Minisatellite Payload) was launched on 15 July 2000 into
 171 a near-circular orbit with an inclination of 87.3° and an initial orbit altitude of 456 km
 172 (Reigber et al., 2002), which decayed to around 250 km in 2010 when the mission re-entered
 173 the atmosphere (see Figure 1). The study of geomagnetic field was one of the objectives
 174 behind this satellite mission. CHAMP carried both scalar and vector magnetometers,
 175 which provided precise measurements of the Earth's magnetic field at the satellite alti-
 176 tude at 1 Hz frequency. The first global survey of magnetic signatures of EPDs includ-
 177 ing a description of their detection in the magnetic field was published by Stolle et al.
 178 (2006). In order to derive the IBP model, the CHAMP magnetic data was re-processed
 179 by the IBI processor as used for the L2 Swarm product to ensure consistency of the de-
 180 tections between Swarm and CHAMP. Since the CHAMP mission provided electron den-
 181 sity measurements at only 15 s resolution, the correlation between magnetic field fluc-
 182 tuations and electron density was disabled in the processor when applied to CHAMP,
 183 because it was not expected to make meaningful contribution as is the case for the high
 184 resolution plasma density data from Swarm. Therefore, all detections in the magnetic
 185 field that exceeded a predefined threshold are identified as an EPD. CHAMP data be-
 186 tween 01 January 2001 and 31 December 2009 have been used to derive the model. The
 187 mean satellite altitude as shown in Figure 1 was around 360 km.

188 2.3 Comparing CHAMP and Swarm data sets

189 Figure 2 shows the probability density of orbits with EPD detections over local time
 190 for the CHAMP and Swarm satellites for the data periods between 01 January 2001 and
 191 31 December 2022. Figure 2a shows CHAMP data applied to a detection threshold of
 192 0.15 nT for EPDs as implemented for the Swarm IBI processor, but without confirma-
 193 tion through correlation with electron density. In Figure 2c, results for the Swarm satel-
 194 lites are shown under the same conditions as for Figure 2a but the EPDs detected by
 195 Swarm A,B,C satellites have been additionally confirmed by correlation with concurrent
 196 electron density measurements. In Figure 2c, the probability density of EPDs rapidly
 197 increases after 18LT, peaks between 20LT and 22LT and then gradually decreases. Very
 198 few EPDs are detected after 02LT. This behaviour is well known from several other in-
 199 dependent satellite observations (e.g., Gentile et al., 2006b; Xiong et al., 2010). For the

200 IBP model, we use the Swarm data that have been processed with a 0.15 nT detection
 201 threshold for EPDs and simultaneously correlated with electron density measurements
 202 as shown in Figure 2c. The probability density based on CHAMP data with the same
 203 threshold of 0.15 nT shows a flatter distribution with a maximum around 22LT and still
 204 relatively high values after 02LT in Figure 2a. The relatively large number of EPD de-
 205 tectations between 02LT and 06LT for CHAMP, are detections with similar frequency and
 206 amplitude to EPDs but do not have corresponding signatures in electron density. Thus,
 207 the histogram is smeared out and we obtain a lower local maximum. Figure 2b shows
 208 the distribution of EPD detection for CHAMP but with a higher detection threshold of
 209 0.25 nT. This resulting histogram shows reduced detections of EPDs beyond 02LT and
 210 a higher probability density between 20-24LT, which is more consistent with observa-
 211 tions of EPDs dedections including the correlation between the magnetic field and plasma
 212 density. Additionally, when the correlations to electron density is not considered for EPDs
 213 detected from Swarm satellites, the probability distribution shown in Figure 2d resem-
 214 bles more closely with the EPD probability distribution shown for CHAMP with 0.25 nT
 215 detection threshold in Figure 2b than with the EPD probability distribution for 0.15 nT
 216 detection threshold shown in Figure 2a.

217 For these reasons, the EPD detection thresholds as applied for Figures 2b and 2d
 218 have been chosen for CHAMP and Swarm data, respectively, to develop the IBP model.
 219 Additionally, we only consider CHAMP and Swarm data during periods with solar flux
 220 indices $F10.7 \geq 80$ s.f.u and during geomagnetic quiet periods with Hp30 indices ≤ 3 (Tap-
 221 ping, 2013; Yamazaki et al., 2022). Setting a threshold for F10.7 improved the perfor-
 222 mance of the IBP model, e.g., reduces the overestimation of low occurrence rates (see
 223 also chapter 5.2).

224 3 Model development

225 The IBP model describing the EPD occurrence probability is based on parameter
 226 estimations for functions of local time, longitude, day of year (doy) and solar flux level.
 227 The model development is based on the assumption that an EPD has a random life-time
 228 and that it is detected by the satellite at an arbitrary time during the EPD's existence.
 229 We further assume that the time of appearance of an EPD at a certain region has a con-
 230 stant mean and a given variance and may be modeled by a Gaussian distributed ran-
 231 dom variable. The random lifetime of an EPD is described by an exponential distributed
 232 random variable. For each EPD, a realization of its lifetime and its starting time is cre-
 233 ated which defines its time of existence. In addition, we make use of a Poisson distributed
 234 random variable to account for the possibility that several EPDs may appear at the same
 235 location during the same night. The parameters of the IBP model are described in Ta-
 236 ble 1.

237 We make use of a half orbit integration of the IBI dataset (either ascending or de-
 238 scending), since no latitudinal distribution is modeled and it is also uncertain, if two de-
 239 tectations during one pass are in fact the same EPD. If no EPD is detected along the satel-
 240 lite pass, the pass is flagged with 0. If at least one EPB is detected in the subset of IBI
 241 data, the pass is flagged with 1. Our model process is thus also constructed to have two

Table 1. The basic model parameters used in the IBP model.

Parameter (units)	Influence	Distribution
$\mu(hours), \sigma(hours)$	mean and variance start-time	Gaussian distribution
λ	plasma bubble intensity	Poisson distribution
$\frac{1}{\gamma}(hours)$	expected lifetime of bubbles	Exponential distribution

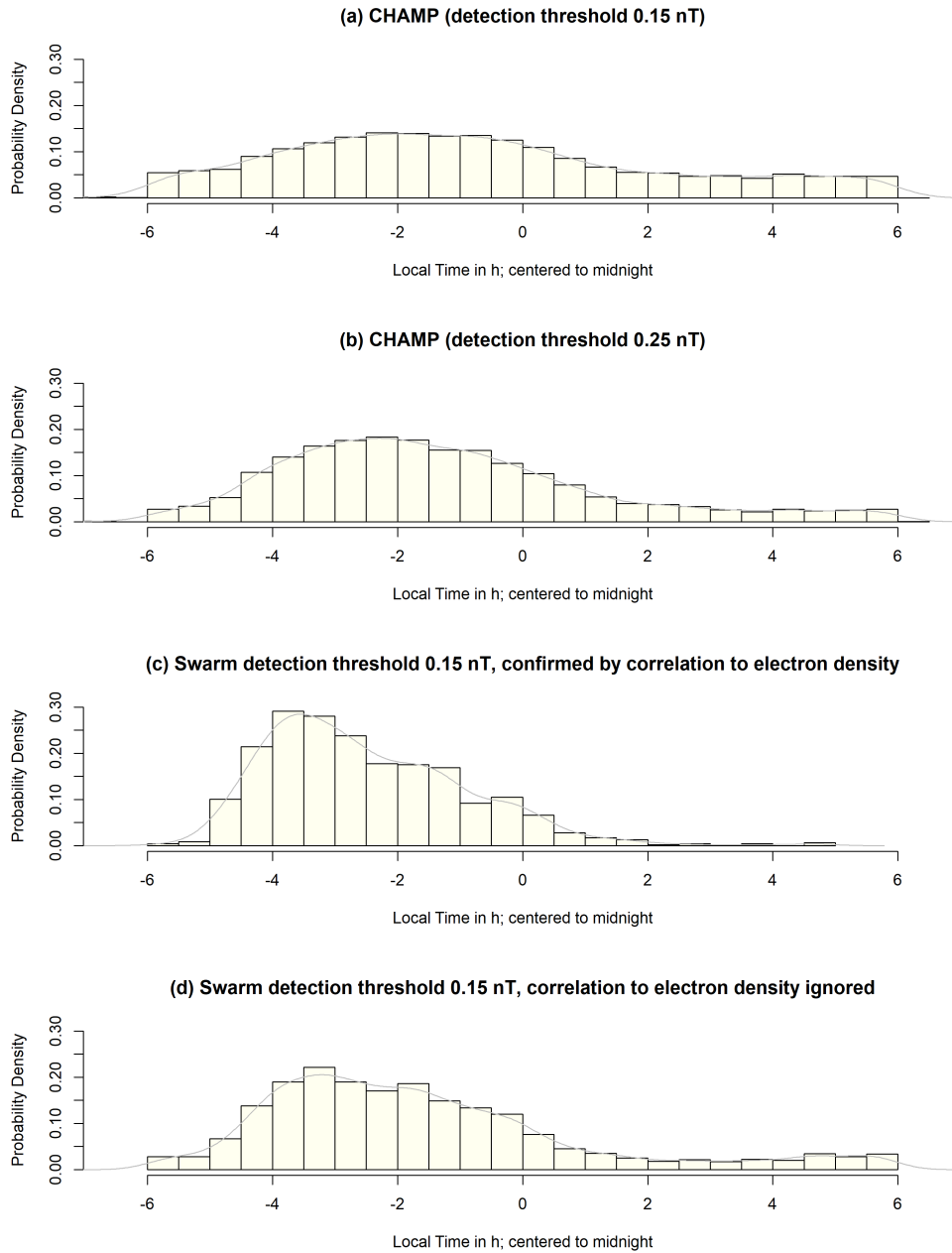


Figure 2. Probability density of orbits with EPD detections over local time for the CHAMP and Swarm missions.

242 states, 0 and 1. To obtain a state of 1, a minimum one bubble has to appear before the
 243 satellite pass and in addition when adding its life time it has to exceed the time of the
 244 satellite pass. This may be expressed in the following way. Let $T_0^{(i)}$, $L^{(i)}$, $i \in \mathbb{N}$ be the
 245 series of realizations of appearance times (in local time) and lifetimes of EPDs and the
 246 number of EPDs in that night be given by n . Then, we can define a process $X(t)$, which
 247 describes the state of an EPD being detected during a satellite pass or not. For a given
 248 local time, t , we can write:

$$X(t) = \mathbb{1} \left\{ \sum_{i=1}^n \mathbb{1}(T_0^{(i)} < t) \cdot \mathbb{1}(T_0^{(i)} + L^{(i)} > t) \right\} \quad (1)$$

249 The first term of Equation 1 indicates the appearance of the bubble before time,
 250 t , while the second term indicates if its end of existence is past t . The function $\mathbb{1}$ rep-
 251 represents the indicator function and takes a value of 1 if the condition is valid, else the in-
 252 dicator function is 0. This function represents a process that has two states 0 and 1. A
 253 state of 0 denotes that no EPD is detected while a state of 1 denotes that a minimum
 254 of one EPD is detected in the satellite pass at the given time, which is identical to the
 255 integration of the dataset. Given the distributions (see Table 1), we can rewrite the prob-
 256 ability, P , of obtaining a flag of 1 as

$$\begin{aligned} P[X(t) = 1] &= 1 - P[X(t) = 0] \\ &= 1 - P \left[\left\{ \sum_{i=1}^{N_\lambda} \mathbb{1}(T_0^{(i)} < t) \cdot \mathbb{1}(T_0^{(i)} + L^{(i)} > t) \right\} = 0 \right] \\ &= 1 - e^{\lambda \cdot I(t, \gamma, \mu, \sigma)} \end{aligned} \quad (2)$$

257 where the integral $I(t, \gamma, \mu, \sigma)$ is defined as,

$$I(t, \gamma, \mu, \sigma) = \int_{-\infty}^t \frac{1}{\sqrt{2\pi}\sigma} e^{\left(\frac{-(x-\mu)^2}{2\sigma^2}\right)} (-e^{-\gamma(t-x)}) dx \quad (3)$$

258 The complete derivation of Equation 2 can be found in Appendix A.

259 3.1 Modeling the bubble intensity parameter

260 Several parameters of this IBP model are not a single number, but are functions
 261 dependent on season, longitude, and F10.7. The global bubble intensity parameter, λ ,
 262 varies with season, with the F10.7 index and also with longitude and can be represented
 263 as,

$$\lambda = \lambda(\text{doy}, \text{lon}, F10.7) \quad (4)$$

264 The longitudinal distribution of λ is given by a probability density function $\phi_{\text{month}}(\text{lon})$
 265 for each month. Since the integral of a probability density function equals 1, $\phi_{\text{month}}(\text{lon})$
 266 is not affecting the global intensity. Thus we may separate into global intensity and lon-
 267 gitudinal distribution. The global bubble intensity consists of three parts, a constant (C_1),
 268 a linear fit including the F10.7 index ($C_2 \cdot F10.7$) and an estimated function $g_{\text{osc}}(\text{doy})$
 269 to describe the seasonal dependency. Eventually λ can be written as

$$\lambda(\text{doy}, \text{lon}, F10.7) = (g_{\text{osc}}(\text{doy}) + C_1 + C_2 \cdot F10.7) \cdot \phi_{\text{month}}(\text{lon}) \quad (5)$$

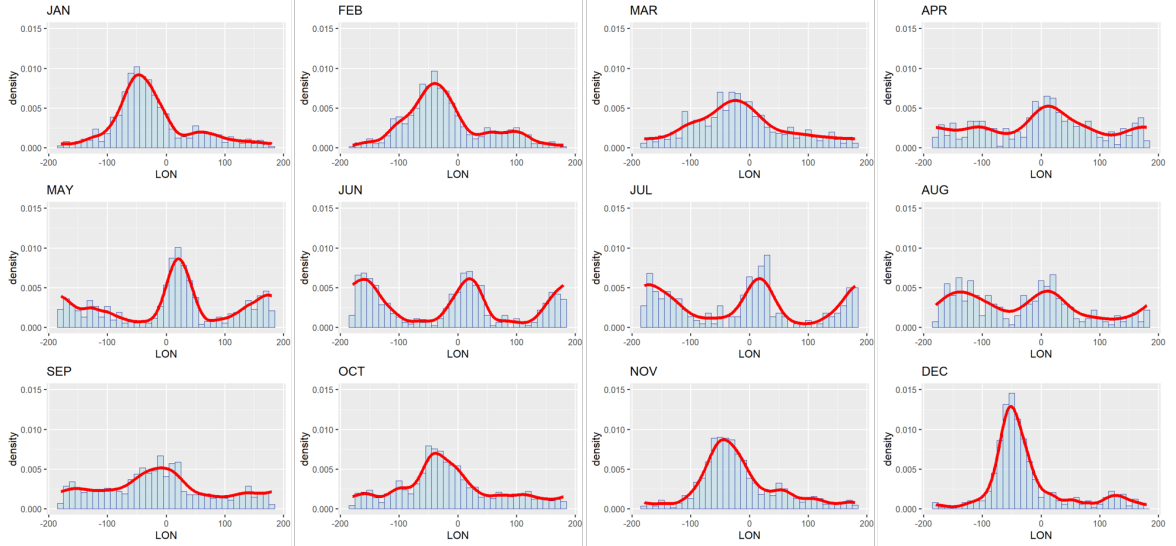


Figure 3. Monthly longitudinal densities obtained using kernel density estimation is shown in solid red lines. The histogram in the background shows the monthly probability density of EPDs as a function of longitude.

270

By substituting λ in Equation 2, we obtain

$$P[X(t) = 1] = 1 - e^{(g_{osc}(doy) + C_1 + C_2 \cdot F10.7) \cdot \phi_{month}(lon) \cdot I(t, \gamma, \mu, \sigma)} \quad (6)$$

271

3.2 Modeling the longitudinal probability density and timeshift functions

272

273 The longitudinal probability density function $\phi_{month}(lon)$ is obtained using a kernel
 274 density estimation method. The density is estimated from the normalized EPD de-
 275 tectations of the CHAMP and Swarm satellites. To determine the optimal bandwidth for
 276 the kernel density estimation of $\phi_{month}(lon)$, we apply a direct plug-in method devel-
 277 oped by Sheather & Jones (1991). To validate this choice of bandwidth, cross-validation
 278 was carried out where the bandwidth selected by employing the Sheather & Jones (1991)
 279 method was found to be optimal. We apply this kernel density estimator to the observed
 280 bubbles for each month and arrive at the monthly longitudinal densities, which are shown
 281 in Figure 3. The solid red lines in this figure show the longitudinal variation of $\phi_{month}(lon)$
 282 for each month. Remarkable, already here, are the higher values of $\phi_{month}(lon)$ over the
 283 Atlantic/American sector during the months of November to February and the lower val-
 284 ues during May to August. The histogram shown in blue colour gives the monthly proba-
 285 bility density of EPDs detected from CHAMP and Swarm satellites as a function of lon-
 286 gitude.

287

288

289

290

291

The time of appearance of EPD is modeled in this IBP model using a Gaussian dis-
 tribution with the parameters μ and σ . As it is known that the appearance of EPD may
 vary with season and longitude (see Figure 8, Stolle et al., 2008), this has been taken into
 account by adding a monthly timeshift function depending on longitude, $ts_{month}(lon)$,
 to the parameter μ_0 , which can be expressed as

$$\mu(month, lon) = \mu_0 + ts_{month}(lon) \quad (7)$$

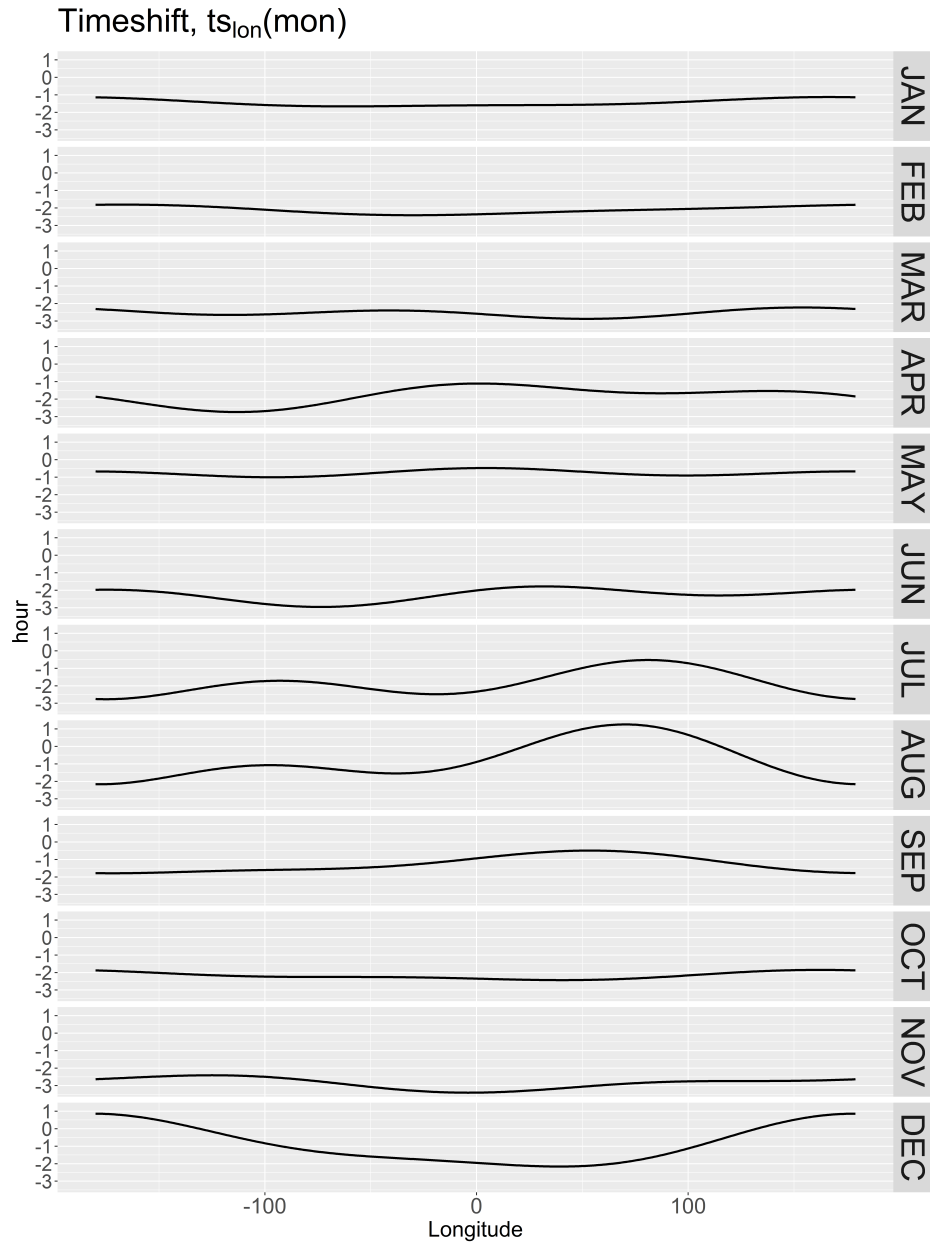


Figure 4. Dependence of monthly timeshift function on longitude. Here in the y-axis, 0 refers to 24 LT.

292 The monthly variation of $ts_{month}(lon)$ as a function of longitude is shown in Fig-
 293 ure 4 where variations of up to 2 hours in $ts_{month}(lon)$ may be observed. The timeshift
 294 is estimated using a least-squares fit for the coefficients of the harmonic function described
 295 below

$$ts_{month}(lon) = t_0 + \sum_1^2 (t_i^{(s)} \sin(i \cdot \frac{lon}{360} \cdot 2\pi)) + (t_i^{(c)} \cos(i \cdot \frac{lon}{360} \cdot 2\pi)) \quad (8)$$

296 The coefficients for the timeshift function can be estimated directly from the local
 297 time and the longitude of the detected EPDs using a least-squares fit, since we as-
 298 sume the lifetime parameter γ to be globally constant. However, the constant t_0 may
 299 be affected, but this can be compensated by the estimation of parameter μ in a follow-
 300 ing step. By expanding $I(t, \gamma, \mu, \sigma)$ using Equation 3 and then substituting $ts_{month}(lon)$
 301 in Equation 6, the model takes the following form:

$$P[X(t) = 1] = 1 - exp \left\{ (g_{osc}(doy) + C_1 + C_2 \cdot F10.7) \cdot \phi_{month}(lon) \right. \\ \left. \cdot \left(\int_{-\infty}^t \frac{1}{\sqrt{2\pi}\sigma} exp \left\{ \frac{-(x - (\mu + ts_{month}(lon)))^2}{2\sigma^2} \right\} (-e^{-\gamma(t-x)} dx) \right) \right\} \quad (9)$$

302 Equation 9 provides a probability for each time, t , which is used to estimate whether
 303 the current data point is an EPD or not. We compare this estimated probability of EPDs
 304 with the observed EPD flag of 0 and 1 in the data and minimize the root mean square
 305 error (RMSE) to estimate the parameters $\mu, \sigma, \gamma, C1$ and $C2$. It is important to note that
 306 since $g_{osc}(doy)$ is determined at a later step, we use λ_{tmp} in place of λ by setting $g_{osc}(doy)$
 307 to 0 in Equation 9 while estimating $\mu, \sigma, \gamma, C1$ and $C2$, where λ_{tmp} is given by

$$\lambda_{tmp} = (C_1 + C_2 \cdot F10.7) \cdot \phi_{month}(lon) \quad (10)$$

308 and

$$RMSE = \sqrt{\frac{1}{n} \sum_{i=1}^n (Flag_i - P_i)^2} \quad (11)$$

309 This RMSE was minimized using a BFGS (Broyden-Fletcher-Goldfarb-Shanno) method.
 310 This minimization method also has the option of passing on boundary conditions. To
 311 ensure that the actual minimum was reached reliably, the minimization was performed
 312 multiple times with randomized starting points.

313 After estimating $\mu, \sigma, \gamma, C1$ and $C2$ using Equation 9, we now estimate $g_{osc}(doy)$,
 314 which is a periodic function that takes the seasonal variability of the intensity of the EPDs
 315 into account. Without including this parameter in λ , the model cannot account for the
 316 well-known seasonal variability of EPDs. To resolve this issue, the residuals between the
 317 number of EPDs that are observed in the data and the number that are estimated by
 318 the model over a 5-day moving period are computed. From these residuals, a least-squares
 319 fit to estimate the coefficients for $g_{osc}(doy)$ is performed. The function $g_{osc}(doy)$ is de-
 320 veloped using a harmonic expansion and reads as

$$g_{osc}(doy) = g_0 + \sum_1^2 (g_i^{(s)} \sin(i \cdot \frac{doy}{365} \cdot 2\pi)) + (g_i^{(c)} \cos(i \cdot \frac{doy}{365} \cdot 2\pi)) \quad (12)$$

Table 2. IBP model coefficients

$C1$	$C2$	$\frac{1}{\gamma}$ (hours)	μ (hours)	σ (hours)
-221.7870	4.3522	1.4121	-1.3386	1.0754

321 In summary, the procedure for solving for the parameters and coefficients of the
322 IBP model follows the following steps:

- 323 1. estimate monthly time-shift coefficients
- 324 2. estimate monthly longitudinal densities
- 325 3. estimate the global coefficients $\mu, \sigma, \gamma, C1$ and $C2$
- 326 4. compute residuals and estimate the coefficients for g_{osc}

327 The values of the coefficients $\mu, \sigma, \gamma, C1$ and $C2$ obtained after minimization are
328 summarized in Table 2.

329 4 Results

330 4.1 Climatology of EPD occurrence derived by the IBP model

331 We first evaluate the IBP model with a constant input value of $F10.7=150$ s.f.u to
332 examine if it is capable of describing the seasonal, longitudinal and localtime distribu-
333 tions of EPDs that has been discussed in earlier works based on CHAMP, Swarm and
334 other LEO satellite missions (e.g., Stolle et al., 2006; Gentile et al., 2006b; Xiong et al.,
335 2010; Aa et al., 2020). The longitudinal and temporal distribution of EPDs along with
336 its occurrence probability are shown in Figure 5 for solstice (June and December) and
337 equinox months (March and September). The IBP model reproduces high occurrence
338 probability of EPDs ranging between 50-90% over the South-American sector (75° - 25° W)
339 and low occurrence probability over the Pacific sector (180° - 120° W) during the Decem-
340 ber solstice. For this period, EPDs over the South American sector arise around 20 LT,
341 peak between 21 and 22 LT and then rapidly decrease after 23 LT, which is consistent
342 with its climatological variations as reported by the earlier independent works cited above.
343 For the March/September equinox months, high occurrence probability of EPDs rang-
344 ing between 50-70% is seen to extend eastward from the South American sector over to
345 the West African sector (75° W- 30° E). The temporal variation of EPDs for these peri-
346 ods differ slightly as the occurrence probability of EPDs peaks around 21 LT during March
347 and an hour later, around 22 LT, during September. Significant EPDs occurrence prob-
348 ability reaching about 40% is also seen over the Pacific sector during equinox months.
349 The IBP model records high occurrence probability of EPDs during June over the African
350 (25° W- 50° E) and Pacific sectors in pre-midnight hours while minima is recorded over
351 the South American sector.

352 4.2 Dependence of EPD occurrence on solar activity

353 The occurrence of EPDs shows an evident dependence on solar activity with EPDs
354 being more prevalent under solar maximum than solar minimum conditions (e.g., Gen-
355 tile et al., 2006a). The performance of the IBP model in simulating the variability of EPDs
356 under varying solar flux conditions is given in Figure 6. On the basis of the F10.7 index,
357 we assess whether the IBP model reproduces a more frequent occurrence of EPDs un-
358 der solar maximum than solar minimum conditions. We present the monthly global oc-
359 currence rate of EPDs derived from the IBP model with F10.7 index ranging between
360 80 and 200 s.f.u with increasing steps of 40 s.f.u in Figure 6. The monthly global occur-

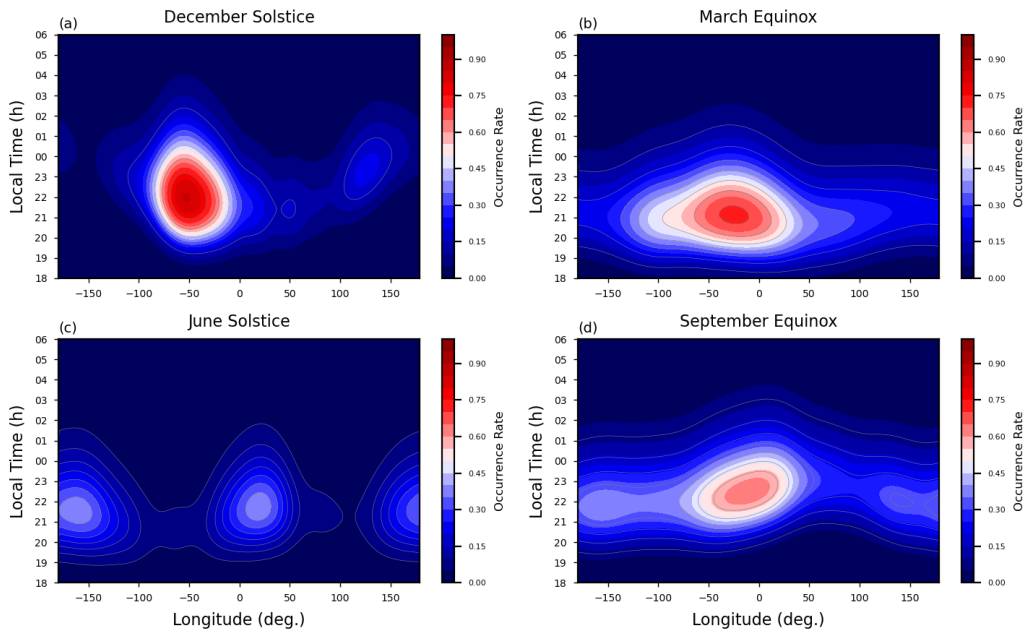


Figure 5. Occurrence probability of EPDs presented as a function of longitude and local time predicted by the IBP model at a constant F10.7 index of 150 s.f.u during (a) December, (b) March, (c) June, and (d) September.

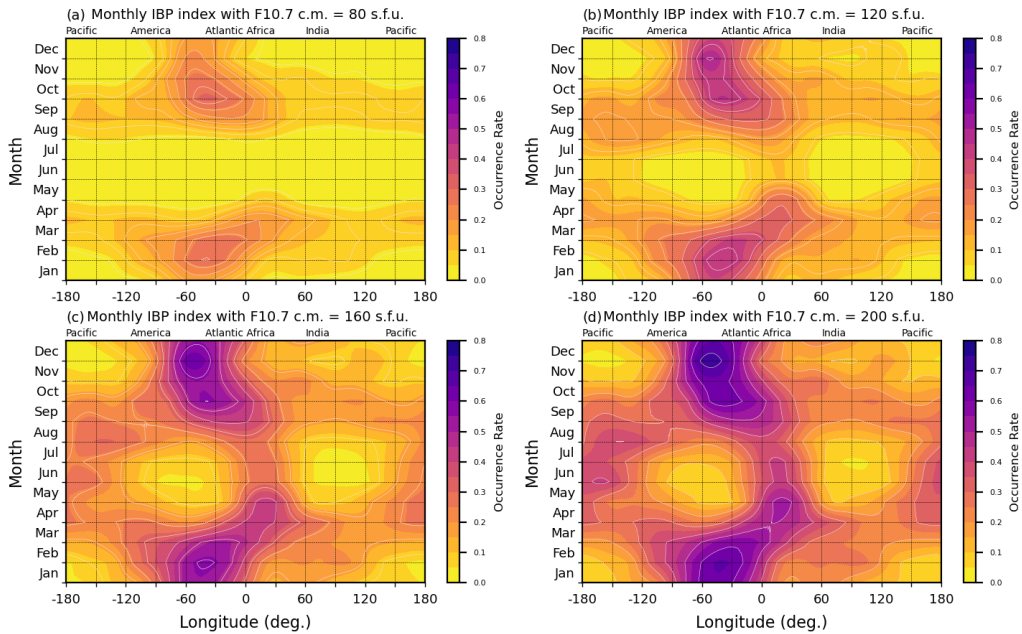


Figure 6. Occurrence probability of EPDs presented as a function of longitude and month predicted by the IBP model at F10.7 values of (a) 80 s.f.u, (b) 120 s.f.u, (c) 160 s.f.u and (d) 200 s.f.u.

361 rence rate from the IBP model, referred henceforth as monthly IBP index, is derived for
 362 a fixed value of F10.7 for all integer longitudes at a resolution of 5° at the middle of each
 363 month and averaged between 19 and 01 LT. We find that the IBP model reproduces the
 364 expected positive linear relationship between EPD occurrence rates and F10.7 index. The
 365 monthly IBP index generally retains negligible probabilities for F10.7 at 80 s.f.u except
 366 in the America-Atlantic-Africa sector during the equinoxes and solstice periods. How-
 367 ever, with increasing F10.7 levels, the monthly IBP indices begin to show significant prob-
 368 abilities as EPDs become more prevalent. Besides, with F10.7 at 120 s.f.u and above,
 369 the seasonal and longitudinal variations of the EPD occurrence rates are particularly well-
 370 characterized by the IBP model compared to its climatology (e.g., Gentile et al., 2006a)
 371 with monthly IBP index reaching highest rates around the equinoxes and winter solstice
 372 in the America-Atlantic-Africa region and lowest rates during November-February in the
 373 Pacific sector and during May-July in the America-Atlantic and Indian sectors. The re-
 374 sults from the IBP model showing a dependence on F10.7 levels compares well with the
 375 findings of Gentile et al. (2006b), which showed the climatology of EPD based on 15 years
 376 of plasma density measurements using the Defense Meteorological Satellite Program (DMSP)
 377 satellites.

378 5 Assessment of the IBP model

379 5.1 Overview of assessment methods

380 The performance of probabilistic predictions by models developed for space weather
 381 phenomena have been typically quantified in the literature using skill scores and rela-
 382 tive (receiver) operating characteristic (ROC) curves (e.g., Barnes et al., 2016; Murray
 383 et al., 2017; Nishizuka et al., 2020). A skill score is generally defined as the measure of
 384 accuracy of forecasts of interest relative to the accuracy of the forecasts produced by some
 385 reference procedure (Murphy, 1988). A generic skill score takes the following form,

$$Skill\ Score = \frac{A_{forecast} - A_{reference}}{A_{perfect} - A_{reference}} \quad (13)$$

386 where $A_{forecast}$ is the accuracy of the forecasting method under consideration, $A_{perfect}$
 387 is the accuracy of a perfect forecast and $A_{reference}$ is the accuracy of a reference method
 388 or the accuracy that is attainable by chance, which is usually chosen to be the clima-
 389 tology of the considered event. For probabilistic forecasts, a measure of accuracy is the
 390 mean square error (MSE), which can be used to calculate $A_{forecast}$ as shown in Barnes
 391 et al. (2016) in the following way,

$$A_{forecast} = MSE(p_f, o) = \langle (p_f - o)^2 \rangle \quad (14)$$

392 where p_f is the forecast probability from the considered method and o is the value
 393 for binary outcomes ($o = 0$ for non event, $o = 1$ for an event). The MSE for a per-
 394 fect forecast, $A_{perfect}$, is 0.

395 In this work, we use the Brier Skill Score (BSS) (Wilks, 1995) for evaluating the
 396 probability forecasting capability of the IBP model. BSS is calculated from the Brier score
 397 (BS) and climatological Brier score (BS_c) by using the following equation,

$$BSS = \frac{BS - BS_c}{0 - BS_c} \quad (15)$$

398 where $BS = MSE(p_f, o)$ and $BS_c = MSE(\langle o \rangle, o)$. BSS can be complemented
 399 by a reliability diagram, which compares the forecast probabilities with the observed fre-
 400 quency of the events.

401 The quality of the probability forecasts are also assessed by using the ROC curve,
 402 which relates the true positive rate (TPR) or the probability of detection (POD) against
 403 the corresponding false alarm rate (FAR) (e.g., Swets, 1973; Mason, 1982). TPR or POD
 404 and FAR can be easily understood in case of a binary categorical forecasting system us-
 405 ing a 2×2 contingency table (see Table 3).

Table 3. 2×2 contingency table for a binary, categorical forecasting system

Observation	Forecasts		
	Positive	Negative	Total
Event	True Positive (TP)	False Negative (FN)	TP+FN
Nonevent	False Positive (FP)	True Negative (TN)	FP+TN
Total	TP+FP	FN+TN	N=TP+FP+FN+TN

406 From the contingency table, POD and FAR are defined as follows (e.g., Mason, 1982)

$$POD = \frac{TP}{TP + FN} \quad \text{and} \quad FAR = \frac{FP}{FP + TN} \quad (16)$$

407 Probabilistic forecasts can be converted to binary, categorical forecasts by select-
 408 ing a probability threshold, P_{th} , such that any forecast probability over the threshold
 409 is considered to be a forecast for an event, and anything less is considered to be a fore-
 410 cast for a non-event. By varying this threshold value, contingency tables along with cor-
 411 responding POD and FAR can be determined for every P_{th} and based on these result-
 412 ing POD and FAR values, a ROC curve can be obtained. As POD and FAR are the axes
 413 of the ROC curve and they range between 0 and 1, the ROC curve for no-skill forecasts
 414 coincides with the 45° line from the origin passing through (0,0) and (1,1) with POD and
 415 FAR being equal. For a perfect forecast, the ROC curve connects the points (0,0), (0,1)
 416 and (1,1) with the values of POD and FAR being 1 and 0, respectively. The accuracy
 417 of binary, categorical forecasts can be determined using standard skill scores and can be
 418 summarized by the ROC Skill Score (ROCSS), also known as the Gini coefficient $G1$ (e.g.,
 419 Jolliffe & Stephenson, 2012) and by the Hanssen and Kuiper’s Discriminant (H&KSS),
 420 also known as the true skill statistic (TSS) or the Peirce skill score (e.g., Hanssen & Kuipers,
 421 1965; Murhy, 1993). $G1 = 2 \times A - 1.0$ where A is the area under the ROC curve, and
 422 $G1 = 1.0$ denotes a perfect score. H&KSS can be written as,

$$H\&KSS = POD - FAR \quad (17)$$

423 H&KSS takes into account the success due to random guessing and it ranges be-
 424 tween -1 and +1. A score of +1 indicates perfect agreement between predictions and ob-
 425 servations while a score of 0 or less indicate no-skill forecasting capability. As H&KSS
 426 can be sensitive to P_{th} , we also calculate the Gini coefficient to present a concise sum-
 427 mary of the assessment of the IBP model.

428 5.2 Model evaluation

429 We use one year of recent IBI index data from the Swarm A, B and C satellites be-
 430 tween July 2022 and June 2023 for the purpose of IBP model validation. During this pe-
 431 riod, the total number of orbits with and without EPD for each Swarm satellite are sum-
 432 marized in Table 4. For each orbit of the satellite, we first compute the EPD occurrence

433 probability from the IBP model for all longitude and local time that the satellite tra-
 434 verses. These probability outputs are then used to derive the maximum EPD occurrence
 435 probability for each satellite orbit. With different choices of probability threshold, P_{th} ,
 436 we predict using this derived maximum EPD occurrence probability whether each satel-
 437 lite orbit contains or not contains EPD. The contingency tables for binary, categorical
 438 forecasts of EPD is then created by varying P_{th} and compared with the observed IBI data
 439 set. We chose a threshold step of 0.02 resulting in covering the P_{th} levels between 0 and
 440 1. Thereafter, POD and FAR values are calculated for different contingency tables and
 441 ROC curves are generated for Swarm A, B and C satellites. These ROC curves are pre-
 442 sented in the upper panels of Figure 7 and are used to visualize H&KSS. When P_{th} is
 443 set to 1, no EPD detections are forecasted and hence TP=FP=0, which corresponds to
 444 the point (0,0) on the ROC curves. When P_{th} is set to 0, all detections are forecasted
 445 as EPD and hence FN=TN=0, which corresponds to the point (1,1) on the ROC curves.
 446 For Figures 7a-7c, we find that ROC curves stay well above the 45° no-skill forecast line
 447 shown here in dashed green color. The ROC curves also stay close to the FAR=0 while
 448 the POD rises, which suggests that the IBP model well forecasts EPD events. For Swarm
 449 satellites A, B and C, we find that H&KSS maximizes at at similar values, e.g., when
 450 P_{th} equals 0.22, 0.18 and 0.18, respectively, which is shown through dashed vertical black
 451 lines. H&KSS values reach 0.66, 0.73 and 0.65 for satellites A, B and C, respectively, which
 452 suggests that the forecasting capability of the IBP model is significantly better than a
 453 no-skill forecast. The Gini coefficient for Swarm A, B and C satellites are 0.80, 0.86 and
 454 0.80, respectively.

Table 4. Total number of orbits with and without EPD for each Swarm satellite between July 2022 and June 2023

Satellite	# of orbits		
	Total	with EPDs	without EPDs
A	3165	334	2831
B	3294	262	3032
C	3189	357	2832

455 In the lower panels of Figure 7, the BSS score and reliability plots that accompany
 456 it are presented for the three Swarm satellites. The BSS for Swarm A, B and C equal
 457 0.317, 0.320 and 0.316, respectively. The reliability plots are constructed by first select-
 458 ing probability intervals and then the frequency of observed events within each interval
 459 is estimated using the method described in Wheatland (2005). This observed frequency
 460 is then plotted against the predicted probability and the error bars are estimated based
 461 on the number of events that lie within each interval. On a reliability plot, perfect pre-
 462 diction corresponds to a 45° line when observed frequency equals the predicted proba-
 463 bility, which is plotted here using the dashed green lines in Figure 7d-f. Points lying above
 464 this line indicate underprediction while points located below this line imply overpredic-
 465 tion. We find that the IBP model underestimates the occurrence frequency of EPD when
 466 the predicted probability exceeds 0.7 for all three satellites. Below this predicted proba-
 467 bility value, the model slightly overestimates the occurrence frequency of EPD for all
 468 three satellites. We found, that the overestimation for low occurrence rates increases with
 469 the amount of data of very low solar flux. These times are usually free of EPD detec-
 470 tions in the topside F region. A reasonable results as shown in Figure 7, was found for
 471 a cutoff of $F10.7 \leq 80$ s.f.u.. In summary, the model slightly underestimates the EPD
 472 occurrence at occasions of high EPD probability and it slightly overestimates the EPD
 473 occurrence of low EPD probability. The performance of the IBP model based on the eval-
 474 uation metrics used here above is summarized in Table 5.

Table 5. IBP model performance based on the evaluation metrics for Swarm data between July 2022 and June 2023

Satellite	H&KSS (P_{th})	G1	BSS
A	0.66 (0.22)	0.80	0.317
B	0.73 (0.18)	0.86	0.320
C	0.65 (0.18)	0.80	0.316

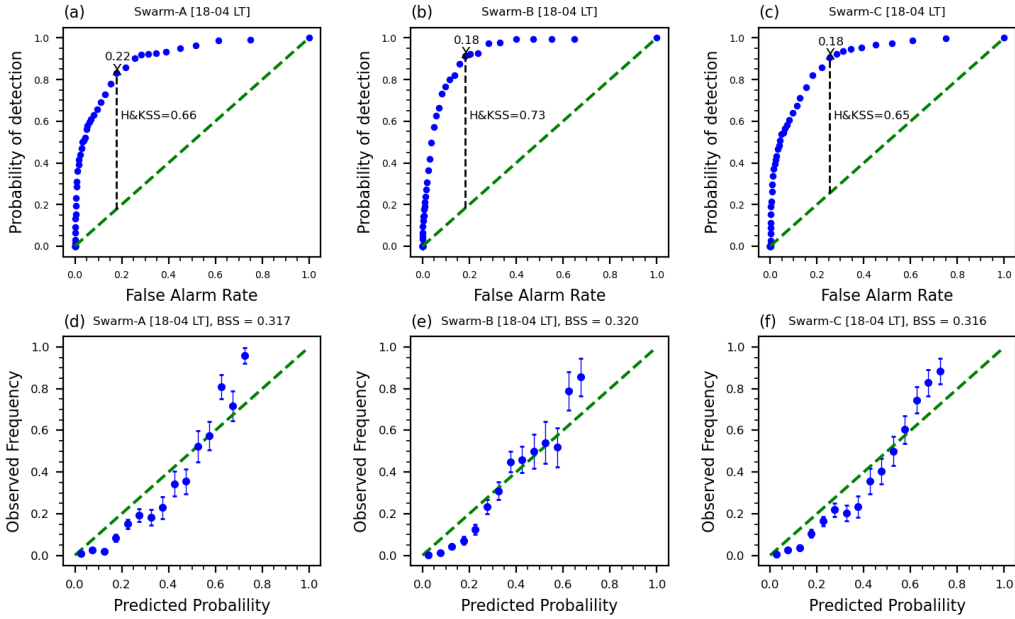


Figure 7. The top panels of the figure (a-c) show receiver operating characteristic (ROC) plots depicting the probability of detection as a function of the false alarm rate by varying the threshold above which an EPD is forecasted. In this case the maximum H&KSS occurs for $p = 0.22, 0.18, 0.18$ for Swarm A, B and C, respectively and is indicated by a dashed vertical line. The random classifier line of the ROC plots is denoted in dashed green colors. The bottom panels (d-f) show reliability plots in which the observed frequency of EPDs is plotted as a function of the forecast probability. Perfect reliability occurs when all points lie on the diagonal ($x=y$) line. The error bars are based on the sample sizes in each relevant bin.

6 Application of the IBP model

The IBP model estimates the occurrence probability of post-sunset equatorial plasma irregularities between 0 (EPDs not at all expected to occur) and 1 (EPDs are fully expected to occur) for a given longitude, local time, day of year, and solar flux value. The performance of the IBP model has been assessed as an estimate largely exceeding a non-skilled forecast in section 5. Thus, the model can be used to predict IBP occurrence with reasonable confidence. The model forward code is publicly made available, as being an official L2 product of the Swarm mission as given at https://swarmhandbook.earth.esa.int/catalogue/SW_IBP_CLI_2_. The forward model code itself and its documentations are available at Gitlab via <https://igit.iap-kborn.de/ibp/ibp-model>. The model code is provided in Python and is also available as a Python package. The model

486 coefficients will be updated with time, when more Swarm observations will be available.
 487 A yearly update is anticipated. Updates will be declared in the Gitlab documentation.

488 Besides the consideration of the assessment results given in section 5, the user of
 489 the IBP model shall be aware of the following constraints. The IBP model

- 490 • estimates the EPD occurrence rate at altitudes between 350 and 500 km, and does
 491 not give information on EPDs which do not reach these altitudes.
- 492 • is not recommended to be applied for solar flux indices $F_{10.7} \leq 80$ s.f.u. and $F_{10.7} \geq 200$ s.f.u..
- 493 • does not predict EPD occurrence depending on latitude. It provides the EPD oc-
 494 currence for a user-defined longitude, but integrated over latitude.

495 7 Conclusions

496 In this study, we have presented the IBP model by explaining its derivation, its as-
 497 sessment, and giving recommendations for its application. The main findings of this study
 498 are summarized below:

- 499 • The IBP model is a statistical climatological model for predicting the occurrence
 500 probability of F region EPDs for a given local time, solar radio flux, day of year,
 501 and longitude.
- 502 • It fully captures the climatology and solar flux dependence of EPDs at altitudes
 503 between 350 and 500 km. The model especially performs well in the American/Atlantic
 504 sector during December solstice and increased solar activity conditions, which is
 505 encouraging as this region and this season is a hotspot for EPDs.
- 506 • Based on one year of recent Swarm magnetic data, which constitutes as partly non-
 507 trained data set for the assessment, the IBP model has been evaluated and var-
 508 ious evaluation metrics have been presented. The IBP model shows improved pre-
 509 diction capability compared to climatological forecasts with moderate skill scores.
 510 With the addition of more recent Swarm data, e.g., by updating the model pa-
 511 rameters, it is expected that the skill scores and accuracy of the IBP model en-
 512 hances further.
- 513 • The IBP model is publicly made available at [https://igit.iap-kborn.de/ibp/
 514 ibp-model](https://igit.iap-kborn.de/ibp/ibp-model).

515 8 Open Research

516 The CHAMP magnetic data set used in this paper (Rother & Michaelis, 2019) can
 517 be freely downloaded using the following ftp link, [ftp://anonymous@isdcftp.gfz-potsdam
 518 .de/champ/](ftp://anonymous@isdcftp.gfz-potsdam.de/champ/). How to access the data and data citations can be found under [https://
 519 isdc.gfz-potsdam.de/champ-isdc/access-to-the-champ-data/](https://isdc.gfz-potsdam.de/champ-isdc/access-to-the-champ-data/). The Swarm data
 520 set is publicly available from the European Space Agency website using the following web-
 521 site link <https://earth.esa.int/eogateway/missions/swarm/data>. The IBP model
 522 is publicly available with the Gitlab link <https://igit.iap-kborn.de/ibp/ibp-model>.
 523 The F10.7 index is accessible at [https://lasp.colorado.edu/lisird/data/noaa_radio
 524 _flux](https://lasp.colorado.edu/lisird/data/noaa_radio_flux). The Hp30 index (Matzka et al., 2022) is provided at [https://kp.gfz-potsdam
 525 .de/en/hp30-hp60](https://kp.gfz-potsdam.de/en/hp30-hp60). All data sets and software are freely available from the stated links
 526 without the need for user registration. The CHAMP magnetic data set and the Hp30
 527 index are published under licence CC BY 4.0.

528 Acknowledgments

529 This work has been partly supported by Swarm DISC activities funded by ESA under
 530 contract no. 4000109587/13/I-NB.

531 **Appendix A Derivation of Equation 2**

$$\begin{aligned}
P[X(t) = 1] &= 1 - P[X(t) = 0] \\
&= 1 - P \left[\left\{ \sum_{i=1}^{N_\lambda} \mathbb{1}(T_0^{(i)} < t) \cdot \mathbb{1}(T_0^{(i)} + L^{(i)} > t) \right\} = 0 \right] \\
&= 1 - \sum_{i=1}^{\infty} e^{-\lambda} \frac{\lambda^k}{k!} P \left[\mathbb{1}(T_0^{(1)} < t) \cdot \mathbb{1}(T_0^{(1)} + L^{(1)} > t) = 0 \right]^i \\
&= 1 - \sum_{i=1}^{\infty} e^{-\lambda} \frac{\lambda^k}{k!} (1 - P \left[\mathbb{1}(T_0^{(1)} < t) \cdot \mathbb{1}(T_0^{(1)} + L^{(1)} > t) = 1 \right])^i \\
&= 1 - \sum_{i=1}^{\infty} e^{-\lambda} \frac{\lambda^k}{k!} (P \left[T_0^{(1)} > t \right] + P \left[T_0^{(1)} + L^{(1)} < t \right])^i \\
&= 1 - e^{-\lambda} \cdot e^{\lambda \cdot (P \left[T_0^{(1)} > t \right] + P \left[T_0^{(1)} + L^{(1)} < t \right])} \tag{A1} \\
&= 1 - e^{\lambda \cdot (P \left[T_0^{(1)} > t \right] + P \left[T_0^{(1)} + L^{(1)} < t \right] - 1)} \\
&= 1 - e^{\lambda \cdot (-P \left[T_0^{(1)} < t \right] + P \left[T_0^{(1)} + L^{(1)} < t \right])} \\
&= 1 - e^{\lambda \cdot (-\int_{-\infty}^t \frac{1}{\sqrt{2\pi}\sigma} e^{\frac{-(x-\mu)^2}{2\sigma^2}} dx + \int_{-\infty}^t \frac{1}{\sqrt{2\pi}\sigma} e^{\frac{-(x-\mu)^2}{2\sigma^2}} P \left[L^1 < t-x \right] dx)} \\
&= 1 - e^{\lambda \cdot (-\int_{-\infty}^t \frac{1}{\sqrt{2\pi}\sigma} e^{\frac{-(x-\mu)^2}{2\sigma^2}} dx + \int_{-\infty}^t \frac{1}{\sqrt{2\pi}\sigma} e^{\frac{-(x-\mu)^2}{2\sigma^2} (1 - e^{-\gamma \cdot (t-x)})} dx)} \\
&= 1 - e^{\lambda \cdot \left(\int_{-\infty}^t \frac{1}{\sqrt{2\pi}\sigma} e^{\frac{-(x-\mu)^2}{2\sigma^2}} (-e^{-\gamma(t-x)}) dx \right)} \\
&= 1 - e^{\lambda \cdot I(t, \gamma, \mu, \sigma)}
\end{aligned}$$

532 **References**

- 533 Aa, E., Zhang, S.-R., Coster, A. J., Erickson, P. J., & Rideout, W. (2023). Multi-
534 instrumental analysis of the day-to-day variability of equatorial plasma bubbles.
535 *Frontiers in Astronomy and Space Sciences*, 10. doi: <https://doi.org/10.3389/fspas.2023.1167245>
536
- 537 Aa, E., Zou, S., & Liu, S. (2020). Statistical Analysis of Equatorial Plasma Irreg-
538 ularities Retrieved From Swarm 2013–2019 Observations. *Journal of Geophysical*
539 *Research: Space Physics*, 125(4), e2019JA027022. doi: <https://doi.org/10.1029/2019JA027022>
540
- 541 Abdu, M. A. (2019). Day-to-day and short-term variabilities in the equatorial
542 plasma bubble/spread F irregularity seeding and development. *Progress in Earth*
543 *and Planetary Science*, 6(1), 11. doi: <https://doi.org/10.1186/s40645-019-0258-1>
544
- 545 Abdu, M. A., de Medeiros, R. T., Bittencourt, J. A., & Batista, I. S. (1983). Ver-
546 tical ionization drift velocities and range type spread F in the evening equatorial
547 ionosphere. *Journal of Geophysical Research: Space Physics*, 88(A1), 399-402. doi:
<https://doi.org/10.1029/JA088iA01p00399>
- 548 Balsley, B. B., Haerendel, G., & Greenwald, R. A. (1972). Equatorial spread F:
549 Recent observations and a new interpretation. *Journal of Geophysical Research*
550 *(1896-1977)*, 77(28), 5625-5628. doi: <https://doi.org/10.1029/JA077i028p05625>
- 551 Barnes, G., Leka, K. D., Schrijver, C. J., Colak, T., Qahwaji, R., Ashamari, O. W.,
552 ... Wagner, E. L. (2016). A comparison of flare forecasting methods. I. Results
553 from the “All-Clear” workshop. *The Astrophysical Journal*, 829(2), 89. doi:
554 <https://10.3847/0004-637X/829/2/89>
- 555 Basu, S., Basu, S., Huba, J., Krall, J., McDonald, S. E., Makela, J. J., ... Groves,
556 K. (2009). Day-to-day variability of the equatorial ionization anomaly and

- 557 scintillations at dusk observed by GUVI and modeling by SAMI3. *Journal of*
 558 *Geophysical Research: Space Physics*, 114(A4). doi: [https://doi.org/10.1029/](https://doi.org/10.1029/2008JA013899)
 559 2008JA013899
- 560 Burke, W. J., Gentile, L. C., Huang, C. Y., Valladares, C. E., & Su, S. Y. (2004).
 561 Longitudinal variability of equatorial plasma bubbles observed by DMSP and
 562 ROCSAT-1. *Journal of Geophysical Research: Space Physics*, 109(A12). doi:
 563 <https://doi.org/10.1029/2004JA010583>
- 564 Carter, B. A., Yizengaw, E., Retterer, J. M., Francis, M., Terkildsen, M., Marshall,
 565 R., ... Zhang, K. (2014). An analysis of the quiet time day-to-day variability
 566 in the formation of postsunset equatorial plasma bubbles in the Southeast Asian
 567 region. *Journal of Geophysical Research: Space Physics*, 119(4), 3206-3223. doi:
 568 <https://doi.org/10.1002/2013JA019570>
- 569 Chou, M.-Y., Pedatella, N. M., Wu, Q., Huba, J. D., Lin, C. C. H., Schreiner,
 570 W. S., ... Yue, J. (2020). Observation and Simulation of the Development
 571 of Equatorial Plasma Bubbles: Post-Sunset Rise or Upwelling Growth? *Jour-*
 572 *nal of Geophysical Research: Space Physics*, 125(12), e2020JA028544. doi:
 573 <https://doi.org/10.1029/2020JA028544>
- 574 Clemesha, B., & Wright, R. (1966). Spread-F and its Effects upon Radio Wave
 575 Propagation and Communications. *P. Newman, Téchnivision. England*, 3.
- 576 Dabas, R. S., Singh, L., Lakshmi, D. R., Subramanyam, P., Chopra, P., & Garg,
 577 S. C. (2003). Evolution and dynamics of equatorial plasma bubbles: Relation-
 578 ships to ExB drift, postsunset total electron content enhancements, and equa-
 579 torial electrojet strength. *Radio Science*, 38(4). doi: [https://doi.org/10.1029/](https://doi.org/10.1029/2001RS002586)
 580 2001RS002586
- 581 Das, S. K., Patra, A. K., & Niranjana, K. (2021). On the Assessment of Day-To-Day
 582 Occurrence of Equatorial Plasma Bubble. *Journal of Geophysical Research: Space*
 583 *Physics*, 126(5), e2021JA029129. doi: <https://doi.org/10.1029/2021JA029129>
- 584 Fagundes, P. R., Sahai, Y., Batista, I. S., Abdu, M. A., Bittencourt, J. A., & Taka-
 585 hashi, H. (1999). Observations of day-to-day variability in precursor signatures to
 586 equatorial F-region plasma depletions. *Annales Geophysicae*, 17(8), 1053-1063.
 587 doi: <https://10.1007/s00585-999-1053-x>
- 588 Farley, D. T., Balsey, B. B., Woodman, R. F., & McClure, J. P. (1970). Equa-
 589 torial spread F: Implications of VHF radar observations. *Journal of Geophys-*
 590 *ical Research (1896-1977)*, 75(34), 7199-7216. doi: [https://doi.org/10.1029/](https://doi.org/10.1029/JA075i034p07199)
 591 JA075i034p07199
- 592 Fejer, B. G., Scherliess, L., & de Paula, E. R. (1999). Effects of the vertical plasma
 593 drift velocity on the generation and evolution of equatorial spread F. *Journal of*
 594 *Geophysical Research: Space Physics*, 104(A9), 19859-19869. doi: [https://doi.org/](https://doi.org/10.1029/1999JA900271)
 595 10.1029/1999JA900271
- 596 Friis-Christensen, E., Lühr, H., & Hulot, G. (2006). Swarm: A constellation to study
 597 the Earth's magnetic field. *Earth, Planets and Space*, 58(4), 351-358. doi: [https://](https://doi.org/10.1186/BF03351933)
 598 doi.org/10.1186/BF03351933
- 599 Fukao, S., Yokoyama, T., Tayama, T., Yamamoto, M., Maruyama, T., & Saito, S.
 600 (2006). Eastward traverse of equatorial plasma plumes observed with the Equa-
 601 torial Atmosphere Radar in Indonesia. *Annales Geophysicae*, 24(5), 1411-1418.
 602 Retrieved from <https://angeo.copernicus.org/articles/24/1411/2006/> doi:
 603 10.5194/angeo-24-1411-2006
- 604 Gentile, L. C., Burke, W. J., & Rich, F. J. (2006a). A climatology of equatorial
 605 plasma bubbles from DMSP 1989-2004. *Radio Science*, 41(5). doi: [https://doi](https://doi.org/10.1029/2005RS003340)
 606 [.org/10.1029/2005RS003340](https://doi.org/10.1029/2005RS003340)
- 607 Gentile, L. C., Burke, W. J., & Rich, F. J. (2006b). A global climatology for equa-
 608 torial plasma bubbles in the topside ionosphere. *Annales Geophysicae*, 24(1), 163-
 609 172. doi: <https://doi.org/10.5194/angeo-24-163-2006>
- 610 Gentile, L. C., Burke, W. J., Roddy, P. A., Retterer, J. M., & Tsunoda, R. T.

- 611 (2011). Climatology of plasma density depletions observed by DMSP in the
 612 dawn sector. *Journal of Geophysical Research: Space Physics*, 116(A3). doi:
 613 <https://doi.org/10.1029/2010JA016176>
- 614 Haerendel, G. (1973). Theory of equatorial spread F. *Space Plasma Physics of Near-*
 615 *Earth Environment*, MPI for Extraterrestrial Physics, Max Planck Society.
- 616 Hanssen, A., & Kuipers, W. (1965). *On the relationship between the frequency of*
 617 *rain and various meteorological parameters. (With reference to the problem of*
 618 *objective forecasting)*. Koninklijk Nederlands Meteorologisch Instituut.
- 619 Huang, C.-S., de La Beaujardiere, O., Roddy, P. A., Hunton, D. E., Liu, J. Y., &
 620 Chen, S. P. (2014). Occurrence probability and amplitude of equatorial iono-
 621 spheric irregularities associated with plasma bubbles during low and moderate
 622 solar activities (2008–2012). *Journal of Geophysical Research: Space Physics*,
 623 119(2), 1186-1199. doi: <https://doi.org/10.1002/2013JA019212>
- 624 Huang, C.-S., & Hairston, M. R. (2015). The postsunset vertical plasma drift and its
 625 effects on the generation of equatorial plasma bubbles observed by the C/NOFS
 626 satellite. *Journal of Geophysical Research: Space Physics*, 120(3), 2263-2275. doi:
 627 <https://doi.org/10.1002/2014JA020735>
- 628 Hysell, D., & Burcham, J. (2002). Long term studies of equatorial spread F us-
 629 ing the JULIA radar at Jicamarca. *Journal of Atmospheric and Solar-Terrestrial*
 630 *Physics*, 64(12), 1531-1543. (Equatorial Aeronomy) doi: [https://doi.org/10.1016/S1364-6826\(02\)00091-3](https://doi.org/10.1016/S1364-6826(02)00091-3)
- 632 Hysell, D. L., Fang, T. W., & Fuller-Rowell, T. J. (2022). Modeling equato-
 633 rial f-region ionospheric instability using a regional ionospheric irregularity
 634 model and wam-ipe. *Journal of Geophysical Research: Space Physics*, 127(9),
 635 e2022JA030513. doi: <https://doi.org/10.1029/2022JA030513>
- 636 Hysell, D. L., Rojas, E., Goldberg, H., Milla, M. A., Kuyeng, K., Valdez, A., ...
 637 Bourne, H. (2021). Mapping irregularities in the postsunset equatorial ionosphere
 638 with an expanded network of hf beacons. *Journal of Geophysical Research: Space*
 639 *Physics*, 126(7), e2021JA029229. doi: <https://doi.org/10.1029/2021JA029229>
- 640 Hysell, D. L., & Seyler, C. E. (1998). A renormalization group approach to esti-
 641 mation of anomalous diffusion in the unstable equatorial F region. *Journal of Geo-*
 642 *physical Research: Space Physics*, 103(A11), 26731-26737. doi: [https://doi.org/10](https://doi.org/10.1029/98JA02616)
 643 [.1029/98JA02616](https://doi.org/10.1029/98JA02616)
- 644 Jolliffe, I. T., & Stephenson, D. B. (2012). *Forecast verification: a practitioner's*
 645 *guide in atmospheric science*. John Wiley & Sons.
- 646 Kelley, M. C. (2009). *The earth's ionosphere: Plasma physics and electrodynamics*.
 647 Academic press.
- 648 Kil, H., & Heelis, R. A. (1998a). Equatorial density irregularity structures at in-
 649 termediate scales and their temporal evolution. *Journal of Geophysical Research:*
 650 *Space Physics*, 103(A3), 3969-3981. doi: <https://doi.org/10.1029/97JA03344>
- 651 Kil, H., & Heelis, R. A. (1998b). Global distribution of density irregularities in the
 652 equatorial ionosphere. *Journal of Geophysical Research: Space Physics*, 103(A1),
 653 407-417. doi: <https://doi.org/10.1029/97JA02698>
- 654 Kil, H., Heelis, R. A., Paxton, L. J., & Oh, S.-J. (2009). Formation of a plasma de-
 655 pletion shell in the equatorial ionosphere. *Journal of Geophysical Research: Space*
 656 *Physics*, 114(A11). doi: <https://doi.org/10.1029/2009JA014369>
- 657 Knudsen, D. J., Burchill, J. K., Buchert, S. C., Eriksson, A. I., Gill, R., Wahlund,
 658 J.-E., ... Moffat, B. (2017). Thermal ion imagers and Langmuir probes in the
 659 Swarm electric field instruments. *Journal of Geophysical Research: Space Physics*,
 660 122(2), 2655-2673. doi: <https://doi.org/10.1002/2016JA022571>
- 661 Kudeki, E., & Bhattacharyya, S. (1999). Postsunset vortex in equatorial F-region
 662 plasma drifts and implications for bottomside spread-F. *Journal of Geophysical*
 663 *Research: Space Physics*, 104(A12), 28163-28170. doi: [https://doi.org/10.1029/](https://doi.org/10.1029/1998JA900111)
 664 [1998JA900111](https://doi.org/10.1029/1998JA900111)

- 665 Li, G., Ning, B., Otsuka, Y., Abdu, M. A., Abadi, P., Liu, Z., . . . Wan, W. (2021,
666 Jan 01). Challenges to Equatorial Plasma Bubble and Ionospheric Scintillation
667 Short-Term Forecasting and Future Aspects in East and Southeast Asia. *Surveys
668 in Geophysics*, 42(1), 201-238. doi: <https://doi.org/10.1007/s10712-020-09613-5>
- 669 Lühr, H., Maus, S., Rother, M., & Cooke, D. (2002). First in-situ observation of
670 night-time F region currents with the CHAMP satellite. *Geophysical Research Let-
671 ters*, 29(10), 127-1-127-4. doi: <https://doi.org/10.1029/2001GL013845>
- 672 Lühr, H., Rother, M., Maus, S., Mai, W., & Cooke, D. (2003). The diamag-
673 netic effect of the equatorial appleton anomaly: Its characteristics and impact
674 on geomagnetic field modeling. *Geophysical Research Letters*, 30(17). doi:
675 <https://doi.org/10.1029/2003GL017407>
- 676 Lühr, H., Xiong, C., Park, J., & Rauberg, J. (2014). Systematic study of
677 intermediate-scale structures of equatorial plasma irregularities in the ionosphere
678 based on CHAMP observations. *Frontiers in Physics*, 2. doi: <https://doi.org/10.3389/fphy.2014.00015>
- 680 Macho, E. P., Correia, E., Spogli, L., & Tadeu de Assis Honorato Muella, M. (2022).
681 Climatology of ionospheric amplitude scintillation on gnss signals at south amer-
682 ican sector during solar cycle 24. *Journal of Atmospheric and Solar-Terrestrial
683 Physics*, 231, 105872. doi: <https://doi.org/10.1016/j.jastp.2022.105872>
- 684 Manju, G., & Aswathy, R. P. (2020). Ionospheric Planetary Wave Activity and Its
685 Role in Equatorial Spread F Day-to-Day Variability. *Journal of Geophysical Re-
686 search: Space Physics*, 125(9), e2020JA027960. (e2020JA027960 2020JA027960)
687 doi: <https://doi.org/10.1029/2020JA027960>
- 688 Martinis, C., Daniell, R., Eastes, R., Norrell, J., Smith, J., Klenzing, J., . . . Burns,
689 A. (2021). Longitudinal Variation of Postsunset Plasma Depletions From
690 the Global-Scale Observations of the Limb and Disk (GOLD) Mission. *Jour-
691 nal of Geophysical Research: Space Physics*, 126(2), e2020JA028510. doi:
692 <https://doi.org/10.1029/2020JA028510>
- 693 Martinis, C., & Mendillo, M. (2007). Equatorial spread F-related airglow depletions
694 at Arecibo and conjugate observations. *Journal of Geophysical Research: Space
695 Physics*, 112(A10). doi: <https://doi.org/10.1029/2007JA012403>
- 696 Mason, I. (1982). A Model for Assessment of Weather Forecasts. *Australian Meteo-
697 rological Magazine*, 30, 291-303.
- 698 Matzka, J., Bronkalla, O., Kervalishvili, G., Rauberg, J., Stolle, C., & Yamazaki,
699 Y. (2022). *Geomagnetic Hpo index. V. 2.0*. [Dataset]. GFZ Data Services. doi:
700 <https://doi.org/10.5880/Hpo.0002>
- 701 Murhy, A. H. (1993). What Is a Good Forecast? An Essay on the Nature of Good-
702 ness in Weather Forecasting. *Weather and Forecasting*, 8(2), 281-293. doi:
703 [https://doi.org/10.1175/1520-0434\(1993\)008<0281:WIAGFA>2.0.CO;2](https://doi.org/10.1175/1520-0434(1993)008<0281:WIAGFA>2.0.CO;2)
- 704 Murphy, J. M. (1988). The impact of ensemble forecasts on predictability. *Quar-
705 terly Journal of the Royal Meteorological Society*, 114(480), 463-493. doi: [https://
706 doi.org/10.1002/qj.49711448010](https://doi.org/10.1002/qj.49711448010)
- 707 Murray, S. A., Bingham, S., Sharpe, M., & Jackson, D. R. (2017). Flare forecasting
708 at the Met Office Space Weather Operations Centre. *Space Weather*, 15(4), 577-
709 588. doi: <https://doi.org/10.1002/2016SW001579>
- 710 Nishizuka, N., Kubo, Y., Sugiura, K., Den, M., & Ishii, M. (2020). Reliable Prob-
711 ability Forecast of Solar Flares: Deep Flare Net-Reliable (DeFN-R). *The Astro-
712 physical Journal*, 899(2), 150. doi: 10.3847/1538-4357/aba2f2
- 713 Olsen, N., Friis-Christensen, E., Floberghagen, R., Alken, P., Beggan, C. D., Chul-
714 liat, A., . . . Visser, P. N. (2013). The Swarm Satellite Constellation Application
715 and Research Facility (SCARF) and Swarm data products. *Earth, Planets and
716 Space*, 65(11), 1189-1200. doi: <https://doi.org/10.5047/eps.2013.07.001>
- 717 Ossakow, S. L. (1981). Spread-F theories-A review. *Journal of Atmospheric and Ter-
718 restrial Physics*, 43(5), 437-452. doi: [https://doi.org/10.1016/0021-9169\(81\)90107](https://doi.org/10.1016/0021-9169(81)90107)

719

-0

720

Park, J., Noja, M., Stolle, C., & Lühr, H. (2013). The Ionospheric Bubble Index deduced from magnetic field and plasma observations onboard Swarm. *Earth, Planets and Space*, *65*(11), 1333-1344. doi: <https://doi.org/10.5047/eps.2013.08.005>

721

722

723

Patra, A. K., & Das, S. K. (2023). On the Upwelling of the F Layer Base and Prediction of Equatorial Plasma Bubble. *Geophysical Research Letters*, *50*(7), e2023GL102803. doi: <https://doi.org/10.1029/2023GL102803>

724

725

726

Rajesh, P. K., Lin, C. C. H., Chen, C. H., Chen, W. H., Lin, J. T., Chou, M. Y., ... You, C. F. (2017). Global equatorial plasma bubble growth rates using ionosphere data assimilation. *Journal of Geophysical Research: Space Physics*, *122*(3), 3777-3787. doi: <https://doi.org/10.1002/2017JA023968>

727

728

729

730

Reddy, S. A., Forsyth, C., Aruliah, A., Smith, A., Bortnik, J., Aa, E., ... Lewis, G. (2023). Predicting Swarm Equatorial Plasma Bubbles via Machine Learning and Shapley Values. *Journal of Geophysical Research: Space Physics*, *128*(6), e2022JA031183. doi: <https://doi.org/10.1029/2022JA031183>

731

732

733

734

Reigber, C., Lühr, H., & Schwintzer, P. (2002). CHAMP mission status. *Advances in Space Research*, *30*(2), 129-134. doi: [https://doi.org/10.1016/S0273-1177\(02\)00276-4](https://doi.org/10.1016/S0273-1177(02)00276-4)

735

736

737

Retterer, J. M., & Roddy, P. (2014). Faith in a seed: on the origins of equatorial plasma bubbles. *Annales Geophysicae*, *32*(5), 485-498. doi: <https://doi.org/10.5194/angeo-32-485-2014>

738

739

740

Rodríguez-Zuluaga, J., Stolle, C., Yamazaki, Y., Lühr, H., Park, J., Scherliess, L., & Chau, J. L. (2019). On the Balance Between Plasma and Magnetic Pressure Across Equatorial Plasma Depletions. *Journal of Geophysical Research: Space Physics*, *124*(7), 5936-5944. doi: <https://doi.org/10.1029/2019JA026700>

741

742

743

744

Rother, M., & Michaelis, I. (2019). *CH-ME-3-MAG - CHAMP 1 Hz Combined Magnetic Field Time Series (Level 3)* [Dataset]. GFZ Data Services. doi: <https://doi.org/10.5880/GFZ.2.3.2019.004>

745

746

747

Sahai, Y., Aarons, J., Mendillo, M., Baumgardner, J., Bittencourt, J., & Takahashi, H. (1994). OI 630 nm imaging observations of equatorial plasma depletions at 16° S dip latitude. *Journal of Atmospheric and Terrestrial Physics*, *56*(11), 1461-1475. doi: [https://doi.org/10.1016/0021-9169\(94\)90113-9](https://doi.org/10.1016/0021-9169(94)90113-9)

748

749

750

751

Sahai, Y., Fagundes, P., & Bittencourt, J. (2000). Transequatorial F-region ionospheric plasma bubbles: solar cycle effects. *Journal of Atmospheric and Solar-Terrestrial Physics*, *62*(15), 1377-1383. doi: [https://doi.org/10.1016/S1364-6826\(00\)00179-6](https://doi.org/10.1016/S1364-6826(00)00179-6)

752

753

754

755

Saito, S., & Maruyama, T. (2006). Ionospheric height variations observed by ionosondes along magnetic meridian and plasma bubble onsets. *Annales Geophysicae*, *24*(11), 2991-2996. doi: <https://doi.org/10.5194/angeo-24-2991-2006>

756

757

758

Saito, S., & Maruyama, T. (2007). Large-scale longitudinal variation in ionospheric height and equatorial spread F occurrences observed by ionosondes. *Geophysical Research Letters*, *34*(16). doi: <https://doi.org/10.1029/2007GL030618>

759

760

761

Sheather, S. J., & Jones, M. C. (1991). A Reliable Data-Based Bandwidth Selection Method for Kernel Density Estimation. *Journal of the Royal Statistical Society: Series B (Methodological)*, *53*(3), 683-690. doi: <https://doi.org/10.1111/j.2517-6161.1991.tb01857.x>

762

763

764

765

Shinagawa, H., Jin, H., Miyoshi, Y., Fujiwara, H., Yokoyama, T., & Otsuka, Y. (2018). Daily and seasonal variations in the linear growth rate of the Rayleigh-Taylor instability in the ionosphere obtained with GAIA. *Progress in Earth and Planetary Science*, *5*(1), 16. doi: <https://doi.org/10.1186/s40645-018-0175-8>

766

767

768

769

Singh, S., Johnson, F. S., & Power, R. A. (1997). Gravity wave seeding of equatorial plasma bubbles. *Journal of Geophysical Research: Space Physics*, *102*(A4), 7399-7410. doi: <https://doi.org/10.1029/96JA03998>

770

771

772

Stolle, C., Lühr, H., & Fejer, B. G. (2008). Relation between the occurrence

- 773 rate of ESF and the equatorial vertical plasma drift velocity at sunset derived
 774 from global observations. *Annales Geophysicae*, 26(12), 3979–3988. doi:
 775 <https://doi.org/10.5194/angeo-26-3979-2008>
- 776 Stolle, C., Lühr, H., Rother, M., & Balasis, G. (2006). Magnetic signatures of equa-
 777 torial spread F as observed by the CHAMP satellite. *Journal of Geophysical Re-*
 778 *search: Space Physics*, 111(A2). doi: <https://doi.org/10.1029/2005JA011184>
- 779 Su, S.-Y., Chao, C. K., & Liu, C. H. (2008). On monthly/seasonal/longitudinal vari-
 780 ations of equatorial irregularity occurrences and their relationship with the post-
 781 sunset vertical drift velocities. *Journal of Geophysical Research: Space Physics*,
 782 113(A5). doi: <https://doi.org/10.1029/2007JA012809>
- 783 Su, S.-Y., Yeh, H. C., & Heelis, R. A. (2001). ROCSAT 1 ionospheric plasma and
 784 electrodynamic instrument observations of equatorial spread F: An early transi-
 785 tional scale result. *Journal of Geophysical Research: Space Physics*, 106(A12),
 786 29153–29159. doi: <https://doi.org/10.1029/2001JA900109>
- 787 Sultan, P. J. (1996). Linear theory and modeling of the Rayleigh-Taylor instability
 788 leading to the occurrence of equatorial spread F. *Journal of Geophysical Research:*
 789 *Space Physics*, 101(A12), 26875–26891. doi: <https://doi.org/10.1029/96JA00682>
- 790 Swets, J. A. (1973). The Relative Operating Characteristic in Psychology: A tech-
 791 nique for isolating effects of response bias finds wide use in the study of perception
 792 and cognition. *Science*, 182(4116), 990–1000.
- 793 Tapping, K. F. (2013). The 10.7cm solar radio flux (f10.7). *Space Weather*, 11(7),
 794 394–406. doi: <https://doi.org/10.1002/swe.20064>
- 795 Tsunoda, R. T. (2005). On the enigma of day-to-day variability in equatorial
 796 spread F. *Geophysical Research Letters*, 32(8). doi: <https://doi.org/10.1029/2005GL022512>
- 797
 798 Tsunoda, R. T., Bubenik, D. M., Thampi, S. V., & Yamamoto, M. (2010). On
 799 large-scale wave structure and equatorial spread F without a post-sunset rise of
 800 the F layer. *Geophysical Research Letters*, 37(7). doi: <https://doi.org/10.1029/2009GL042357>
- 801
 802 Tsunoda, R. T., Saito, S., & Nguyen, T. T. (2018). Post-sunset rise of equatorial
 803 F layer—or upwelling growth? *Progress in Earth and Planetary Science*, 5(1), 22.
 804 doi: <https://doi.org/10.1186/s40645-018-0179-4>
- 805 Tsunoda, R. T., & White, B. R. (1981). On the generation and growth of equa-
 806 torial backscatter plumes 1. Wave structure in the bottomside F layer. *Journal of*
 807 *Geophysical Research: Space Physics*, 86(A5), 3610–3616. doi: [https://doi.org/10](https://doi.org/10.1029/JA086iA05p03610)
 808 [.1029/JA086iA05p03610](https://doi.org/10.1029/JA086iA05p03610)
- 809 Wheatland, M. S. (2005). A statistical solar flare forecast method. *Space Weather*,
 810 3(7). doi: <https://doi.org/10.1029/2004SW000131>
- 811 Wilks, D. (1995). *Forecast verification. Statistical methods in the atmospheric sci-*
 812 *ences*. Academic Press New York, NY, USA.
- 813 Woodman, R. F., & La Hoz, C. (1976). Radar observations of F region equatorial ir-
 814 regularities. *Journal of Geophysical Research (1896-1977)*, 81(31), 5447–5466. doi:
 815 <https://doi.org/10.1029/JA081i031p05447>
- 816 Xiong, C., Park, J., Lühr, H., Stolle, C., & Ma, S. Y. (2010). Comparing
 817 plasma bubble occurrence rates at CHAMP and GRACE altitudes during
 818 high and low solar activity. *Annales Geophysicae*, 28(9), 1647–1658. Re-
 819 trieved from <https://angeo.copernicus.org/articles/28/1647/2010/> doi:
 820 [10.5194/angeo-28-1647-2010](https://doi.org/10.5194/angeo-28-1647-2010)
- 821 Xiong, C., Stolle, C., & Lühr, H. (2016). The Swarm satellite loss of GPS signal
 822 and its relation to ionospheric plasma irregularities. *Space Weather*, 14(8), 563-
 823 577. Retrieved from [https://agupubs.onlinelibrary.wiley.com/doi/abs/10](https://agupubs.onlinelibrary.wiley.com/doi/abs/10.1002/2016SW001439)
 824 [.1002/2016SW001439](https://doi.org/10.1002/2016SW001439) doi: <https://doi.org/10.1002/2016SW001439>
- 825 Xiong, C., Xu, J.-S., Stolle, C., van den Ijssel, J., Yin, F., Kervalishvili, G. N., &
 826 Zangerl, F. (2020). On the Occurrence of GPS Signal Amplitude Degradation for

- 827 Receivers on Board LEO Satellites. *Space Weather*, 18(2), e2019SW002398. doi:
828 <https://doi.org/10.1029/2019SW002398>
- 829 Yamamoto, M., Otsuka, Y., Jin, H., & Miyoshi, Y. (2018). Relationship between
830 day-to-day variability of equatorial plasma bubble activity from GPS scintillation
831 and atmospheric properties from Ground-to-topside model of Atmosphere and
832 Ionosphere for Aeronomy (GAIA) assimilation. *Progress in Earth and Planetary
833 Science*, 5(1), 26. doi: <https://doi.org/10.1186/s40645-018-0184-7>
- 834 Yamazaki, Y., Matzka, J., Stolle, C., Kervalishvili, G., Rauberg, J., Bronkalla, O.,
835 ... Jackson, D. R. (2022). Geomagnetic Activity Index Hpo. *Geophysical Research
836 Letters*, 49(10), e2022GL098860. doi: <https://doi.org/10.1029/2022GL098860>
- 837 Zhan, W., Rodrigues, F. S., & Milla, M. A. (2018). On the Genesis of Postmidnight
838 Equatorial Spread F: Results for the American/Peruvian Sector. *Geophysical Re-
839 search Letters*, 45(15), 7354-7361. doi: <https://doi.org/10.1029/2018GL078822>

1 **An empirical model of the occurrence rate of low**
2 **latitude post-sunset plasma irregularities derived from**
3 **CHAMP and Swarm magnetic observations**

4 **C. Stolle¹, T. A. Siddiqui¹, L. Schreiter^{2,3}, S. K. Das¹, I. Rusch¹, M. Rother³**

5 ¹Leibniz Institute of Atmospheric Physics at the University of Rostock, Kühlungsborn, Germany

6 ²Institute of Geodesy, Technical University of Berlin, Germany

7 ³GFZ German Research Centre for Geosciences, Helmholtz Centre Potsdam, Germany

8 **Key Points:**

- 9 • The IBP model to estimate the occurrence probability of post-sunset equatorial
10 plasma depletions (EPDs) is introduced.
11 • IBP shows high performance in predicting EPD occurrence for longitude, local time,
12 day of year, solar activity, at altitudes of 350-500 km.
13 • The IBP model is publicly available including documentation.

Corresponding author: Claudia Stolle, cstolle@iap-kborn.de

Abstract

The prediction of post-sunset equatorial plasma depletions (EPDs), often called ionospheric plasma bubbles, has remained a challenge for decades. In this study, we introduce the Ionospheric Bubble Probability (IBP), an empirical model to predict the occurrence probability of EPDs derived from 9 years of CHAMP and 8.5 years of Swarm magnetic field measurements. The model predicts the occurrence probability of EPDs for a given longitude, day of year, local time and solar activity, for the altitude range 350-500 km, and low geographic latitudes of $\pm 45^\circ$. IBP has been found to successfully reconstruct the distribution of EPDs as reported in previous studies from independent data. IBP has been further evaluated using one-year of partly untrained data of the Ionospheric Bubble Index (IBI). IBI is a Level 2 product of the Swarm satellite mission used for EPD identification. The relative operating characteristics (ROC) curve shows positive excursion above the no-skill line with Hanssen and Kuiper's Discriminant (H&KSS) score of 0.66, 0.73, and 0.65 at threshold model outputs of 0.22, 0.18, and 0.18 for Swarm A, B, and C satellites, respectively. Additionally, the reliability plots show proximity to the diagonal line with a fairly decent Brier Skill Score (BSS) of 0.317, 0.320, and 0.316 for Swarm A, B, and C respectively. These tests indicate that the model performs significantly better than a no-skill forecast. The IBP model offers a compelling glimpse into the future of EPD forecasting, thus demonstrating its potential to reliably predict EPD occurrences. The IBP model is made publicly available.

Plain Language Summary

[Post-sunset equatorial plasma depletions (EPDs), often called ionospheric plasma bubbles, are a severe threat for reliable radio wave communication. However, their predictability has remained a challenge for the scientific community for decades. In this study, we introduce the Ionospheric Bubble Probability (IBP) model predicting the occurrence probability of post-sunset EPDs for a given longitude, day of year, local time and solar activity, for the altitude range 350-500 km, and low geographic latitudes of $\pm 45^\circ$. To this aim we have used 9 years of CHAMP and 8.5 years of Swarm magnetic field measurements. The IBP model predictions have been found to agree well with climatologies derived from independent data and performs largely better than unskilled forecasts. The IBP model is made publicly available.]

1 Introduction

The post-sunset equatorial and low-latitude ionosphere is susceptible to irregularities associated with F region plasma instability, popularly known as equatorial plasma depletions (EPDs) or ionospheric plasma bubbles. EPDs are regions of steep plasma depletions of several orders of magnitude in electron density with scale sizes ranging from thousands of kilometers down to meters (e.g., D. L. Hysell & Seyler, 1998; Lühr et al., 2014; Su et al., 2001). EPD is believed to be governed by the Rayleigh-Taylor (RT) instability mechanism which operates at the bottomside F region when uplifted during evening time post-sunset rise driven by the pre-reversal enhancement (PRE) of zonal electric field over the dip equator (e.g., Balsley et al., 1972; Haerendel, 1973; Ossakow, 1981; Sultan, 1996; Woodman & La Hoz, 1976; Tsunoda, 2005). The growth of RT instability depends on various ionospheric and thermospheric parameters which include F layer height, zonal (eastward) electric field, bottomside density gradient, meridional wind and perturbation in electron density in the form of seed (e.g., Kelley, 2009). EPDs have been found to exhibit serious threats to radio waves employed for satellite-based communication/navigation applications by producing random fluctuations in signal amplitude and phase known as scintillations. Based on simultaneous observations of plasma density and Global Positioning System (GPS) observables on board the Swarm satellite mission, Xiong et al. (2016, 2020) showed the positive relation between the strengths of EPDs and the severeness of

64 GPS scintillations to even total signal losses. Therefore, predicting EPD occurrence is
 65 of absolute necessity.

66 Although the underlying principle of RT instability is well understood (e.g., Kel-
 67 ley, 2009; Sultan, 1996), understanding the variability in EPD occurrence on a day-to-
 68 day basis continues to be puzzling (e.g., Abdu, 2019; Basu et al., 2009; Carter et al., 2014;
 69 Chou et al., 2020; Manju & Aswathy, 2020; Rajesh et al., 2017; Retterer & Roddy, 2014;
 70 Saito & Maruyama, 2007; Shinagawa et al., 2018; Tsunoda et al., 2010, 2018; Yamamoto
 71 et al., 2018; Das et al., 2021; D. L. Hysell et al., 2022; Patra & Das, 2023). While the
 72 PRE has been found to show a remarkable agreement with EPD occurrence climatolog-
 73 ically (e.g., Clemesha & Wright, 1966; Dabas et al., 2003; Fejer et al., 1999; Gentile et
 74 al., 2006b; D. Hysell & Burcham, 2002; Stolle et al., 2008; Su et al., 2008; Tsunoda, 2005;
 75 Huang & Hairston, 2015), it fails to account on its day-to-day occurrence variability (e.g.,
 76 Abdu et al., 1983; Fukao et al., 2006; Saito & Maruyama, 2006, 2007). Intriguingly, the
 77 growth rate of RT instability has been found to display similar uncertainty (e.g., Shi-
 78 nagawa et al., 2018; Das et al., 2021; Aa et al., 2023). Since the EPD occurrence shows
 79 a large variability both in small- and large-longitudinal scales (e.g., Kil et al., 2009; Kil
 80 & Heelis, 1998a; Martinis et al., 2021; Singh et al., 1997; Stolle et al., 2008; Tsunoda et
 81 al., 2018; Tsunoda & White, 1981), predicting EPD occurrence becomes even more chal-
 82 lenging. Now, it is fairly well understood that missing understanding of the spatio-temporal
 83 behaviour of EPDs, i.e. growth, zonal movement and decay of EPDs, along with the paucity
 84 of continuous measurements of ionospheric parameters is the cause for the challenge in
 85 predicting the day-to-day occurrence variability of EPDs (e.g., Das et al., 2021; Li et al.,
 86 2021; D. L. Hysell et al., 2021; Patra & Das, 2023).

87 While for a long time, traditional methods such as in situ density measurements,
 88 optical imagers and radio wave sounding have been employed to study the day-to-day,
 89 global, and climatological occurrence of EPDs (e.g., Woodman & La Hoz, 1976; Farley
 90 et al., 1970; Kudeki & Bhattacharyya, 1999; Sahai et al., 1994, 2000; Kil & Heelis, 1998b;
 91 Fagundes et al., 1999; Burke et al., 2004; Gentile et al., 2011; Huang et al., 2014; Mar-
 92 tinis & Mendillo, 2007; Das et al., 2021; Aa et al., 2023), subsequently, it has been found
 93 that magnetic field perturbations associated with the diamagnetic current linked to steep
 94 density gradient at the edges of the EPDs can also be used for characterizing EPDs (e.g.,
 95 Lühr et al., 2002; Rodríguez-Zuluaga et al., 2019). Diagnosing EPDs through those sig-
 96 natures in the magnetic field and electron density, Stolle et al. (2006) could successfully
 97 reconstruct the well-known EPB climatology using Flux-Gate Magnetometer (FGM) mea-
 98 surements on-board the Challenging Mini-Satellite Payload (CHAMP) which similarly
 99 were obtained by traditional methods based on plasma density data from other satel-
 100 lite missions (e.g., Gentile et al., 2006b; Xiong et al., 2010). This success led to the in-
 101 troduction of the Ionospheric Bubble Index (IBI) as a standard Level 2 (L2) data prod-
 102 uct of the Swarm mission for the detection of EPDs (e.g., Park et al., 2013). Recently,
 103 Reddy et al. (2023) have utilized a machine learning (ML) based AI Prediction of EPBs
 104 (APE) model to predict the IBI. Their model is derived from 8 years of Swarm data. Fea-
 105 ture analyses revealed that F10.7 is the most important feature in driving the EPB pre-
 106 dictions, whereas latitude is the least.

107 The advantage of EPD climatology derived from in situ observations of polar-orbiting,
 108 Low Earth Orbit (LEO) satellites is their global coverage. However, it should be noted
 109 that these satellites can only detect those irregularities that have evolved into plumes
 110 reaching F region altitudes at or above the F2 peak. Conversely, the bottom-side F re-
 111 gion irregularities, from which plumes may evolve, occur more frequently than F region
 112 plumes are observed, e.g., almost every evening throughout the year and solar cycle, e.g.,
 113 in the American sector. A comprehensive investigation of the irregularity occurrence de-
 114 rived from 20 years of incoherent scatter radar data at the Jicamarca radio observatory
 115 has been provided by Zhan et al. (2018). Accordingly, based on 10 years of ground-based
 116 GPS observations distributed in South America, Macho et al. (2022) indicated some ac-

117 tivity of weak scintillations also during low solar flux years, while moderate or intense
 118 scintillations did only occur during moderate or high solar flux years.

119 This article introduces an empirical model of the occurrence probability of post-
 120 sunset F region EPDs called the Ionospheric Bubble Probability (IBP) model. The IBP
 121 is derived from the detection of magnetic field perturbations associated with EPDs ob-
 122 tained from 9 years of CHAMP and 8.5 years of Swarm observations in the geomagnetic
 123 field. The model predicts the EPD occurrence rate for a given longitude, day of year,
 124 local time and solar activity, for the altitude range 350-500 km, and low geographic lat-
 125 itudes of $\pm 45^\circ$. The occurrence probability is given in the range of 0 to 1, from a 0%
 126 to 100% probability, respectively. The structure of this manuscript goes as following. Sec-
 127 tion 2 provides a description of the data on which the model is based, section 3 describes
 128 the model development methods, section 4 shows the model results, section 5 provides
 129 model validation and discussion, and finally, conclusions are described in section 7. The
 130 forward model code is available from URL: <https://igit.iap-kborn.de/ibp/ibp-model>.

131 2 Data

132 2.1 Swarm satellite mission

133 The Swarm satellite mission is a constellation consisting of three identical satel-
 134 lites Alpha, Bravo and Charlie (A, B and C) launched in November 2013 into near-circular
 135 orbits at an altitude of approximately 490 km (Friis-Christensen et al., 2006; Olsen et
 136 al., 2013). Following orbital maneuvers in April 2014, Swarm A and C fly in a side-by-
 137 side configuration with an inclination of 87.4° and an initial altitude of about 460 km
 138 (see Figure 1), while Swarm B flies at an inclination of 88° and at a higher orbit of ini-
 139 tially about 530 km altitude. Swarm B has been precessing away from the lower pair at
 140 a rate of approximately 1.5 h of local time per year while Swarm A and C precess west-
 141 ward in local time at a rate of 2.7 h per month (Knudsen et al., 2017). The Swarm satel-
 142 lites cover all local times about every 4 months. The satellites carry, among other instru-
 143 ments, a magnetometer package consisting of an Absolute Scalar Magnetometer (ASM)
 144 and a Vector Field Magnetometer (VSM), which provides precise measurements of the
 145 Earth’s magnetic field at the satellite location at 1 Hz frequency. Each satellite also car-
 146 ries a spherical Langmuir probe as part of the Electric Field Instrument (EFI) provid-
 147 ing plasma density observations at 2 Hz frequency (Knudsen et al., 2017).

148 It is known that EPDs can be detected by high-precision magnetometers on board
 149 low earth orbit (LEO) satellites from their diamagnetic effects as regions of locally de-
 150 pleted plasma are characterized by enhanced magnetic field strength (e.g., Lühr et al.,
 151 2003; Stolle et al., 2006; Park et al., 2013). For the Swarm mission, the European Space
 152 Agency (ESA) has introduced the Ionospheric Bubble Index (IBI) as a standard Level 2 (L2)
 153 data product, which is generated from in situ magnetic field and plasma observations
 154 onboard the Swarm satellites and provides detections of EPDs along Swarm orbits. The
 155 IBI product considers not only the characteristic small-scale variations in the magnetic
 156 field to detect EPDs but also the concurrent change in plasma density to confirm these
 157 detected EPDs. The detection threshold of EPDs based on their diamagnetic effects is
 158 set to 0.15 nT. If the correlation between the magnetic field and electron density is suf-
 159 ficiently high (i.e. $p^2 > 0.5$, where p is the pearson correlation coefficient), which confirms
 160 the diamagnetic effect, the magnetic fluctuation is flagged as confirmed EPD. The IBI
 161 product provides a binary indicator for each of the low latitude (below 45°), night side
 162 (18-06LT), 1 Hz magnetic readings whether the measurement is affected by an EPD or
 163 not. If the data quality does not allow for EPD detection, e.g., due to enhanced noise
 164 or too many data gaps, the data is flagged by an integer value larger than 1. The de-
 165 tailed description of the IBI product and of its derivation is outlined in Park et al. (2013).
 166 Swarm data between 01 January 2014 and 31 December 2022 have been used in this study

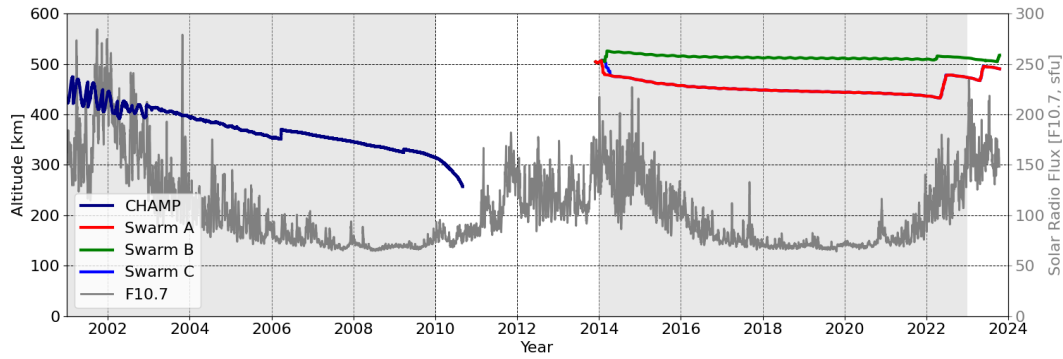


Figure 1. Orbit altitude evolution of the CHAMP and Swarm satellites. The grey line indicates daily values of the F10.7 solar activity index. The light grey areas indicate the times of satellite data which were selected to derive the IBP model.

167 to derive the model. The mean satellite altitudes were around 480 km for Swarm A and
 168 C and 510 km for Swarm B (see Figure 1).

169 2.2 CHAMP satellite mission

170 CHAMP (CHallenging Minisatellite Payload) was launched on 15 July 2000 into
 171 a near-circular orbit with an inclination of 87.3° and an initial orbit altitude of 456 km
 172 (Reigber et al., 2002), which decayed to around 250 km in 2010 when the mission re-entered
 173 the atmosphere (see Figure 1). The study of geomagnetic field was one of the objectives
 174 behind this satellite mission. CHAMP carried both scalar and vector magnetometers,
 175 which provided precise measurements of the Earth’s magnetic field at the satellite alti-
 176 tude at 1 Hz frequency. The first global survey of magnetic signatures of EPDs includ-
 177 ing a description of their detection in the magnetic field was published by Stolle et al.
 178 (2006). In order to derive the IBP model, the CHAMP magnetic data was re-processed
 179 by the IBI processor as used for the L2 Swarm product to ensure consistency of the de-
 180 tections between Swarm and CHAMP. Since the CHAMP mission provided electron den-
 181 sity measurements at only 15 s resolution, the correlation between magnetic field fluc-
 182 tuations and electron density was disabled in the processor when applied to CHAMP,
 183 because it was not expected to make meaningful contribution as is the case for the high
 184 resolution plasma density data from Swarm. Therefore, all detections in the magnetic
 185 field that exceeded a predefined threshold are identified as an EPD. CHAMP data be-
 186 tween 01 January 2001 and 31 December 2009 have been used to derive the model. The
 187 mean satellite altitude as shown in Figure 1 was around 360 km.

188 2.3 Comparing CHAMP and Swarm data sets

189 Figure 2 shows the probability density of orbits with EPD detections over local time
 190 for the CHAMP and Swarm satellites for the data periods between 01 January 2001 and
 191 31 December 2022. Figure 2a shows CHAMP data applied to a detection threshold of
 192 0.15 nT for EPDs as implemented for the Swarm IBI processor, but without confirma-
 193 tion through correlation with electron density. In Figure 2c, results for the Swarm satel-
 194 lites are shown under the same conditions as for Figure 2a but the EPDs detected by
 195 Swarm A,B,C satellites have been additionally confirmed by correlation with concurrent
 196 electron density measurements. In Figure 2c, the probability density of EPDs rapidly
 197 increases after 18LT, peaks between 20LT and 22LT and then gradually decreases. Very
 198 few EPDs are detected after 02LT. This behaviour is well known from several other in-
 199 dependent satellite observations (e.g., Gentile et al., 2006b; Xiong et al., 2010). For the

200 IBP model, we use the Swarm data that have been processed with a 0.15 nT detection
 201 threshold for EPDs and simultaneously correlated with electron density measurements
 202 as shown in Figure 2c. The probability density based on CHAMP data with the same
 203 threshold of 0.15 nT shows a flatter distribution with a maximum around 22LT and still
 204 relatively high values after 02LT in Figure 2a. The relatively large number of EPD de-
 205 tectations between 02LT and 06LT for CHAMP, are detections with similar frequency and
 206 amplitude to EPDs but do not have corresponding signatures in electron density. Thus,
 207 the histogram is smeared out and we obtain a lower local maximum. Figure 2b shows
 208 the distribution of EPD detection for CHAMP but with a higher detection threshold of
 209 0.25 nT. This resulting histogram shows reduced detections of EPDs beyond 02LT and
 210 a higher probability density between 20-24LT, which is more consistent with observa-
 211 tions of EPDs dedections including the correlation between the magnetic field and plasma
 212 density. Additionally, when the correlations to electron density is not considered for EPDs
 213 detected from Swarm satellites, the probability distribution shown in Figure 2d resem-
 214 bles more closely with the EPD probability distribution shown for CHAMP with 0.25 nT
 215 detection threshold in Figure 2b than with the EPD probability distribution for 0.15 nT
 216 detection threshold shown in Figure 2a.

217 For these reasons, the EPD detection thresholds as applied for Figures 2b and 2d
 218 have been chosen for CHAMP and Swarm data, respectively, to develop the IBP model.
 219 Additionally, we only consider CHAMP and Swarm data during periods with solar flux
 220 indices $F10.7 \geq 80$ s.f.u and during geomagnetic quiet periods with Hp30 indices ≤ 3 (Tap-
 221 ping, 2013; Yamazaki et al., 2022). Setting a threshold for F10.7 improved the perfor-
 222 mance of the IBP model, e.g., reduces the overestimation of low occurrence rates (see
 223 also chapter 5.2).

224 3 Model development

225 The IBP model describing the EPD occurrence probability is based on parameter
 226 estimations for functions of local time, longitude, day of year (doy) and solar flux level.
 227 The model development is based on the assumption that an EPD has a random life-time
 228 and that it is detected by the satellite at an arbitrary time during the EPD's existence.
 229 We further assume that the time of appearance of an EPD at a certain region has a con-
 230 stant mean and a given variance and may be modeled by a Gaussian distributed ran-
 231 dom variable. The random lifetime of an EPD is described by an exponential distributed
 232 random variable. For each EPD, a realization of its lifetime and its starting time is cre-
 233 ated which defines its time of existence. In addition, we make use of a Poisson distributed
 234 random variable to account for the possibility that several EPDs may appear at the same
 235 location during the same night. The parameters of the IBP model are described in Ta-
 236 ble 1.

237 We make use of a half orbit integration of the IBI dataset (either ascending or de-
 238 scending), since no latitudinal distribution is modeled and it is also uncertain, if two de-
 239 tectations during one pass are in fact the same EPD. If no EPD is detected along the satel-
 240 lite pass, the pass is flagged with 0. If at least one EPB is detected in the subset of IBI
 241 data, the pass is flagged with 1. Our model process is thus also constructed to have two

Table 1. The basic model parameters used in the IBP model.

Parameter (units)	Influence	Distribution
$\mu(hours), \sigma(hours)$	mean and variance start-time	Gaussian distribution
λ	plasma bubble intensity	Poisson distribution
$\frac{1}{\gamma}(hours)$	expected lifetime of bubbles	Exponential distribution

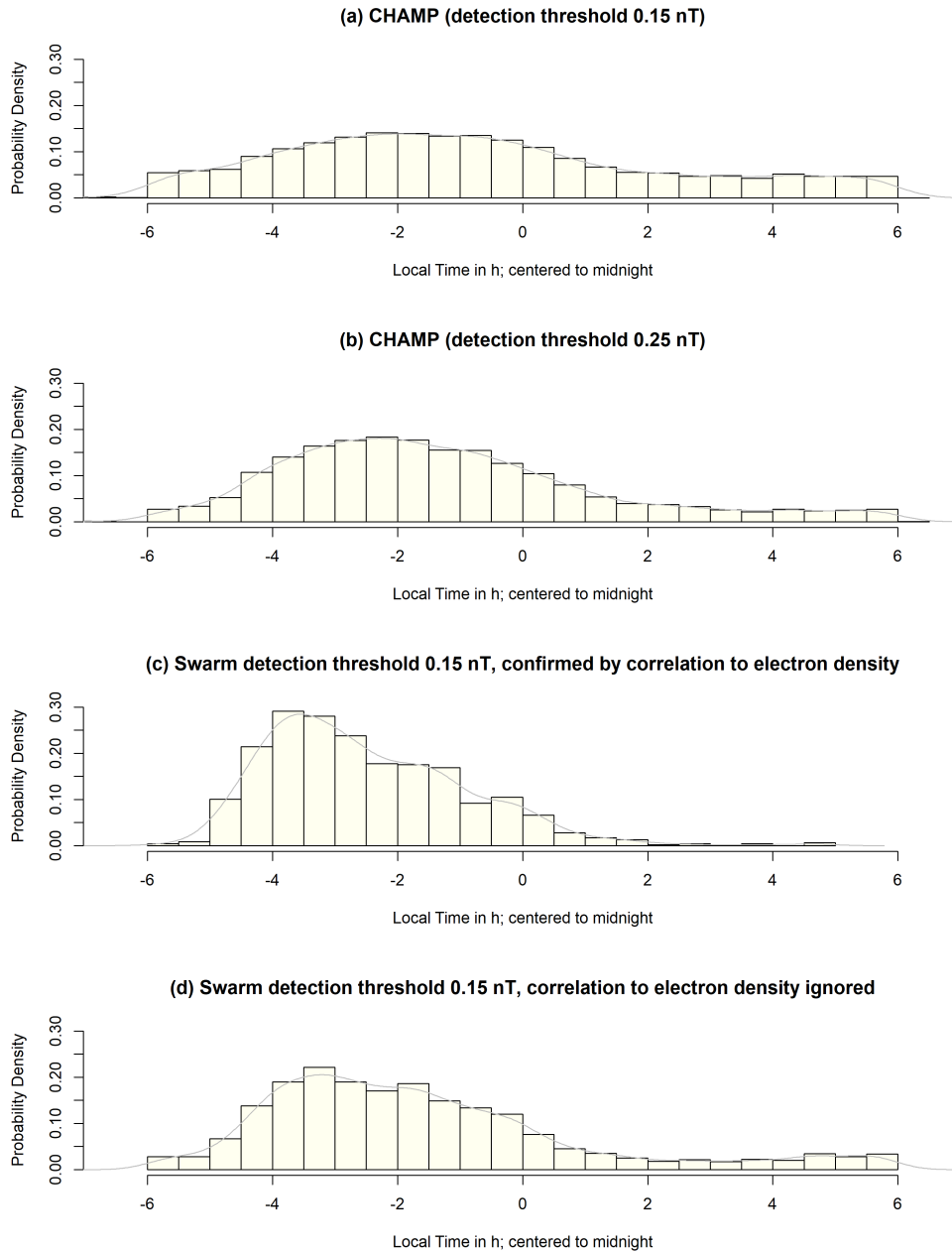


Figure 2. Probability density of orbits with EPD detections over local time for the CHAMP and Swarm missions.

242 states, 0 and 1. To obtain a state of 1, a minimum one bubble has to appear before the
 243 satellite pass and in addition when adding its life time it has to exceed the time of the
 244 satellite pass. This may be expressed in the following way. Let $T_0^{(i)}$, $L^{(i)}$, $i \in \mathbb{N}$ be the
 245 series of realizations of appearance times (in local time) and lifetimes of EPDs and the
 246 number of EPDs in that night be given by n . Then, we can define a process $X(t)$, which
 247 describes the state of an EPD being detected during a satellite pass or not. For a given
 248 local time, t , we can write:

$$X(t) = \mathbb{1} \left\{ \sum_{i=1}^n \mathbb{1}(T_0^{(i)} < t) \cdot \mathbb{1}(T_0^{(i)} + L^{(i)} > t) \right\} \quad (1)$$

249 The first term of Equation 1 indicates the appearance of the bubble before time,
 250 t , while the second term indicates if its end of existence is past t . The function $\mathbb{1}$ rep-
 251 represents the indicator function and takes a value of 1 if the condition is valid, else the in-
 252 dicator function is 0. This function represents a process that has two states 0 and 1. A
 253 state of 0 denotes that no EPD is detected while a state of 1 denotes that a minimum
 254 of one EPD is detected in the satellite pass at the given time, which is identical to the
 255 integration of the dataset. Given the distributions (see Table 1), we can rewrite the prob-
 256 ability, P , of obtaining a flag of 1 as

$$\begin{aligned} P[X(t) = 1] &= 1 - P[X(t) = 0] \\ &= 1 - P \left[\left\{ \sum_{i=1}^{N_\lambda} \mathbb{1}(T_0^{(i)} < t) \cdot \mathbb{1}(T_0^{(i)} + L^{(i)} > t) \right\} = 0 \right] \\ &= 1 - e^{\lambda \cdot I(t, \gamma, \mu, \sigma)} \end{aligned} \quad (2)$$

257 where the integral $I(t, \gamma, \mu, \sigma)$ is defined as,

$$I(t, \gamma, \mu, \sigma) = \int_{-\infty}^t \frac{1}{\sqrt{2\pi}\sigma} e^{\left(\frac{-(x-\mu)^2}{2\sigma^2}\right)} (-e^{-\gamma(t-x)}) dx \quad (3)$$

258 The complete derivation of Equation 2 can be found in Appendix A.

259 3.1 Modeling the bubble intensity parameter

260 Several parameters of this IBP model are not a single number, but are functions
 261 dependent on season, longitude, and F10.7. The global bubble intensity parameter, λ ,
 262 varies with season, with the F10.7 index and also with longitude and can be represented
 263 as,

$$\lambda = \lambda(\text{doy}, \text{lon}, F10.7) \quad (4)$$

264 The longitudinal distribution of λ is given by a probability density function $\phi_{\text{month}}(\text{lon})$
 265 for each month. Since the integral of a probability density function equals 1, $\phi_{\text{month}}(\text{lon})$
 266 is not affecting the global intensity. Thus we may separate into global intensity and lon-
 267 gitudinal distribution. The global bubble intensity consists of three parts, a constant (C_1),
 268 a linear fit including the F10.7 index ($C_2 \cdot F10.7$) and an estimated function $g_{\text{osc}}(\text{doy})$
 269 to describe the seasonal dependency. Eventually λ can be written as

$$\lambda(\text{doy}, \text{lon}, F10.7) = (g_{\text{osc}}(\text{doy}) + C_1 + C_2 \cdot F10.7) \cdot \phi_{\text{month}}(\text{lon}) \quad (5)$$

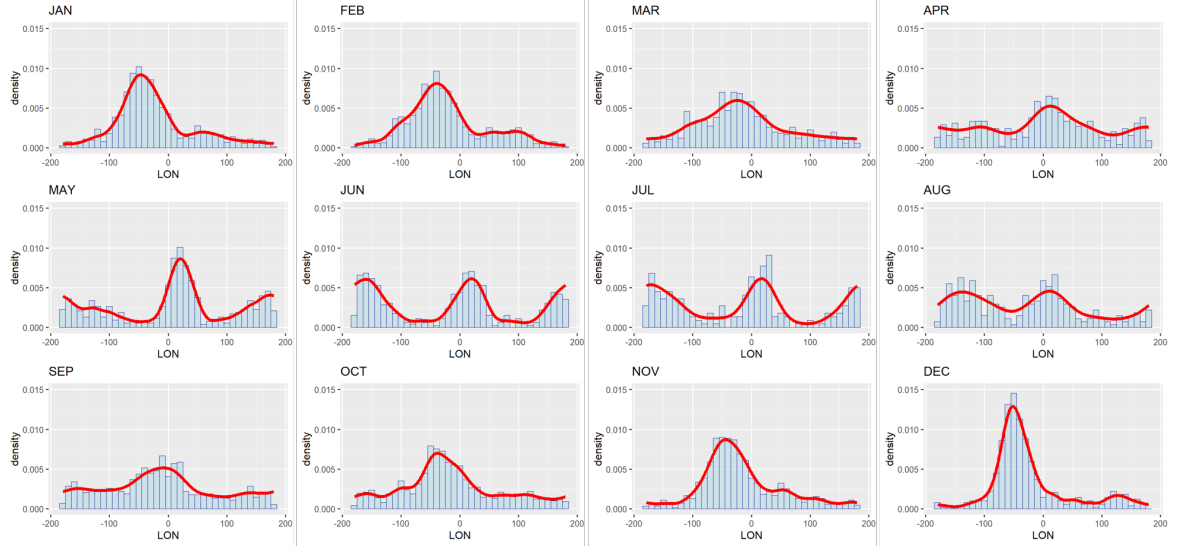


Figure 3. Monthly longitudinal densities obtained using kernel density estimation is shown in solid red lines. The histogram in the background shows the monthly probability density of EPDs as a function of longitude.

270

By substituting λ in Equation 2, we obtain

$$P[X(t) = 1] = 1 - e^{(g_{osc}(doy) + C_1 + C_2 \cdot F10.7) \cdot \phi_{month}(lon) \cdot I(t, \gamma, \mu, \sigma)} \quad (6)$$

271

3.2 Modeling the longitudinal probability density and timeshift functions

272

273 The longitudinal probability density function $\phi_{month}(lon)$ is obtained using a kernel
 274 density estimation method. The density is estimated from the normalized EPD de-
 275 tections of the CHAMP and Swarm satellites. To determine the optimal bandwidth for
 276 the kernel density estimation of $\phi_{month}(lon)$, we apply a direct plug-in method devel-
 277 oped by Sheather & Jones (1991). To validate this choice of bandwidth, cross-validation
 278 was carried out where the bandwidth selected by employing the Sheather & Jones (1991)
 279 method was found to be optimal. We apply this kernel density estimator to the observed
 280 bubbles for each month and arrive at the monthly longitudinal densities, which are shown
 281 in Figure 3. The solid red lines in this figure show the longitudinal variation of $\phi_{month}(lon)$
 282 for each month. Remarkable, already here, are the higher values of $\phi_{month}(lon)$ over the
 283 Atlantic/American sector during the months of November to February and the lower val-
 284 ues during May to August. The histogram shown in blue colour gives the monthly proba-
 285 bility density of EPDs detected from CHAMP and Swarm satellites as a function of lon-
 286 gitude.

287

288

289

290

291

The time of appearance of EPD is modeled in this IBP model using a Gaussian dis-
 tribution with the parameters μ and σ . As it is known that the appearance of EPD may
 vary with season and longitude (see Figure 8, Stolle et al., 2008), this has been taken into
 account by adding a monthly timeshift function depending on longitude, $ts_{month}(lon)$,
 to the parameter μ_0 , which can be expressed as

$$\mu(month, lon) = \mu_0 + ts_{month}(lon) \quad (7)$$

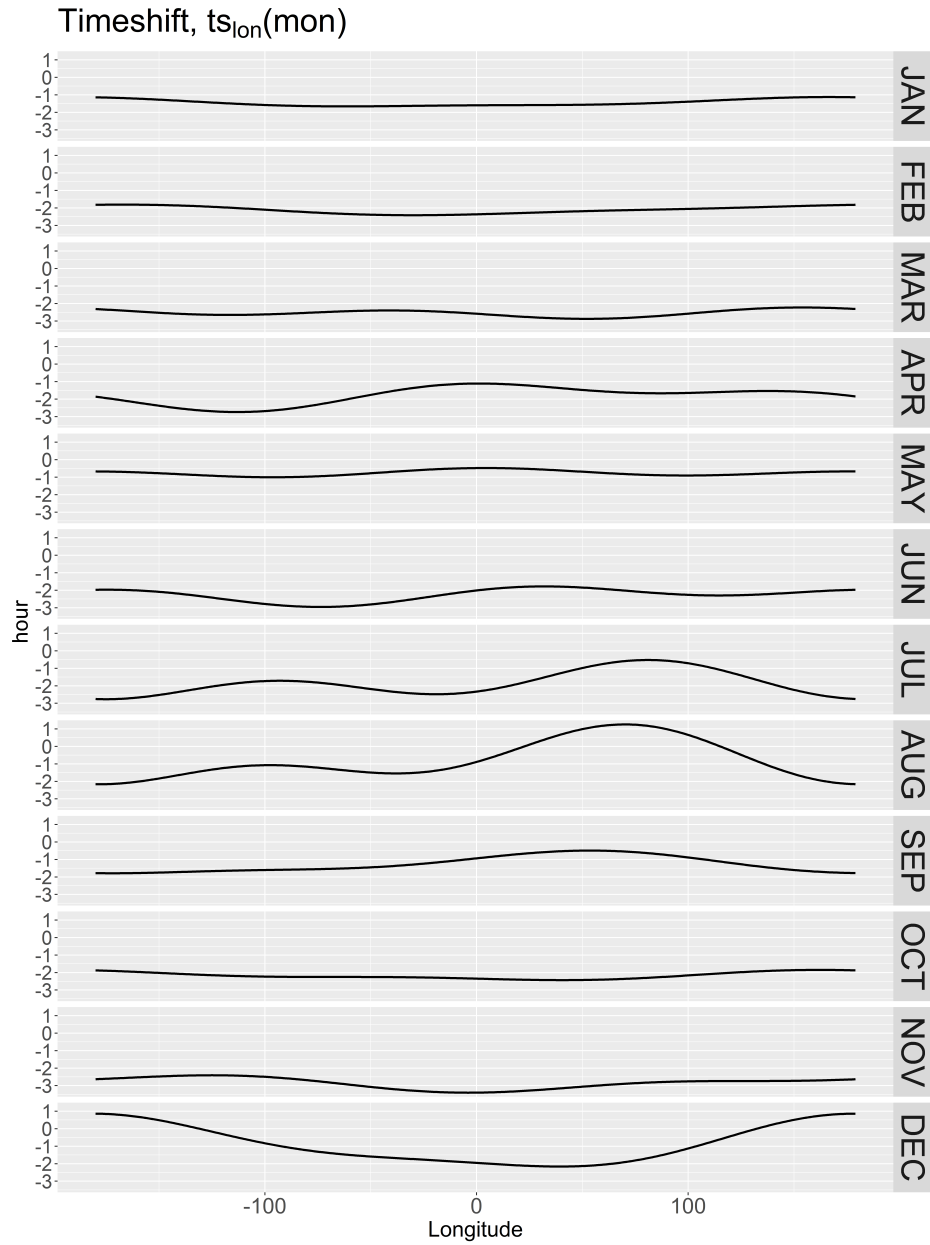


Figure 4. Dependence of monthly timeshift function on longitude. Here in the y-axis, 0 refers to 24 LT.

292 The monthly variation of $ts_{month}(lon)$ as a function of longitude is shown in Fig-
 293 ure 4 where variations of up to 2 hours in $ts_{month}(lon)$ may be observed. The timeshift
 294 is estimated using a least-squares fit for the coefficients of the harmonic function described
 295 below

$$ts_{month}(lon) = t_0 + \sum_1^2 (t_i^{(s)} \sin(i \cdot \frac{lon}{360} \cdot 2\pi)) + (t_i^{(c)} \cos(i \cdot \frac{lon}{360} \cdot 2\pi)) \quad (8)$$

296 The coefficients for the timeshift function can be estimated directly from the local
 297 time and the longitude of the detected EPDs using a least-squares fit, since we as-
 298 sume the lifetime parameter γ to be globally constant. However, the constant t_0 may
 299 be affected, but this can be compensated by the estimation of parameter μ in a follow-
 300 ing step. By expanding $I(t, \gamma, \mu, \sigma)$ using Equation 3 and then substituting $ts_{month}(lon)$
 301 in Equation 6, the model takes the following form:

$$P[X(t) = 1] = 1 - exp \left\{ (g_{osc}(doy) + C_1 + C_2 \cdot F10.7) \cdot \phi_{month}(lon) \right. \\ \left. \cdot \left(\int_{-\infty}^t \frac{1}{\sqrt{2\pi}\sigma} exp \left\{ \frac{-(x - (\mu + ts_{month}(lon)))^2}{2\sigma^2} \right\} (-e^{-\gamma(t-x)} dx) \right) \right\} \quad (9)$$

302 Equation 9 provides a probability for each time, t , which is used to estimate whether
 303 the current data point is an EPD or not. We compare this estimated probability of EPDs
 304 with the observed EPD flag of 0 and 1 in the data and minimize the root mean square
 305 error (RMSE) to estimate the parameters $\mu, \sigma, \gamma, C1$ and $C2$. It is important to note that
 306 since $g_{osc}(doy)$ is determined at a later step, we use λ_{tmp} in place of λ by setting $g_{osc}(doy)$
 307 to 0 in Equation 9 while estimating $\mu, \sigma, \gamma, C1$ and $C2$, where λ_{tmp} is given by

$$\lambda_{tmp} = (C_1 + C_2 \cdot F10.7) \cdot \phi_{month}(lon) \quad (10)$$

308 and

$$RMSE = \sqrt{\frac{1}{n} \sum_{i=1}^n (Flag_i - P_i)^2} \quad (11)$$

309 This RMSE was minimized using a BFGS (Broyden-Fletcher-Goldfarb-Shanno) method.
 310 This minimization method also has the option of passing on boundary conditions. To
 311 ensure that the actual minimum was reached reliably, the minimization was performed
 312 multiple times with randomized starting points.

313 After estimating $\mu, \sigma, \gamma, C1$ and $C2$ using Equation 9, we now estimate $g_{osc}(doy)$,
 314 which is a periodic function that takes the seasonal variability of the intensity of the EPDs
 315 into account. Without including this parameter in λ , the model cannot account for the
 316 well-known seasonal variability of EPDs. To resolve this issue, the residuals between the
 317 number of EPDs that are observed in the data and the number that are estimated by
 318 the model over a 5-day moving period are computed. From these residuals, a least-squares
 319 fit to estimate the coefficients for $g_{osc}(doy)$ is performed. The function $g_{osc}(doy)$ is de-
 320 veloped using a harmonic expansion and reads as

$$g_{osc}(doy) = g_0 + \sum_1^2 (g_i^{(s)} \sin(i \cdot \frac{doy}{365} \cdot 2\pi)) + (g_i^{(c)} \cos(i \cdot \frac{doy}{365} \cdot 2\pi)) \quad (12)$$

Table 2. IBP model coefficients

$C1$	$C2$	$\frac{1}{\gamma}$ (hours)	μ (hours)	σ (hours)
-221.7870	4.3522	1.4121	-1.3386	1.0754

321 In summary, the procedure for solving for the parameters and coefficients of the
 322 IBP model follows the following steps:

- 323 1. estimate monthly time-shift coefficients
- 324 2. estimate monthly longitudinal densities
- 325 3. estimate the global coefficients $\mu, \sigma, \gamma, C1$ and $C2$
- 326 4. compute residuals and estimate the coefficients for g_{osc}

327 The values of the coefficients $\mu, \sigma, \gamma, C1$ and $C2$ obtained after minimization are
 328 summarized in Table 2.

329 4 Results

330 4.1 Climatology of EPD occurrence derived by the IBP model

331 We first evaluate the IBP model with a constant input value of F10.7=150 s.f.u to
 332 examine if it is capable of describing the seasonal, longitudinal and localtime distribu-
 333 tions of EPDs that has been discussed in earlier works based on CHAMP, Swarm and
 334 other LEO satellite missions (e.g., Stolle et al., 2006; Gentile et al., 2006b; Xiong et al.,
 335 2010; Aa et al., 2020). The longitudinal and temporal distribution of EPDs along with
 336 its occurrence probability are shown in Figure 5 for solstice (June and December) and
 337 equinox months (March and September). The IBP model reproduces high occurrence
 338 probability of EPDs ranging between 50-90% over the South-American sector (75-25°W)
 339 and low occurrence probability over the Pacific sector (180-120°W) during the Decem-
 340 ber solstice. For this period, EPDs over the South American sector arise around 20 LT,
 341 peak between 21 and 22 LT and then rapidly decrease after 23 LT, which is consistent
 342 with its climatological variations as reported by the earlier independent works cited above.
 343 For the March/September equinox months, high occurrence probability of EPDs rang-
 344 ing between 50-70% is seen to extend eastward from the South American sector over to
 345 the West African sector (75°W-30°E). The temporal variation of EPDs for these peri-
 346 ods differ slightly as the occurrence probability of EPDs peaks around 21 LT during March
 347 and an hour later, around 22 LT, during September. Significant EPDs occurrence prob-
 348 ability reaching about 40% is also seen over the Pacific sector during equinox months.
 349 The IBP model records high occurrence probability of EPDs during June over the African
 350 (25°W-50°E) and Pacific sectors in pre-midnight hours while minima is recorded over
 351 the South American sector.

352 4.2 Dependence of EPD occurrence on solar activity

353 The occurrence of EPDs shows an evident dependence on solar activity with EPDs
 354 being more prevalent under solar maximum than solar minimum conditions (e.g., Gen-
 355 tile et al., 2006a). The performance of the IBP model in simulating the variability of EPDs
 356 under varying solar flux conditions is given in Figure 6. On the basis of the F10.7 index,
 357 we assess whether the IBP model reproduces a more frequent occurrence of EPDs un-
 358 der solar maximum than solar minimum conditions. We present the monthly global oc-
 359 currence rate of EPDs derived from the IBP model with F10.7 index ranging between
 360 80 and 200 s.f.u with increasing steps of 40 s.f.u in Figure 6. The monthly global occur-

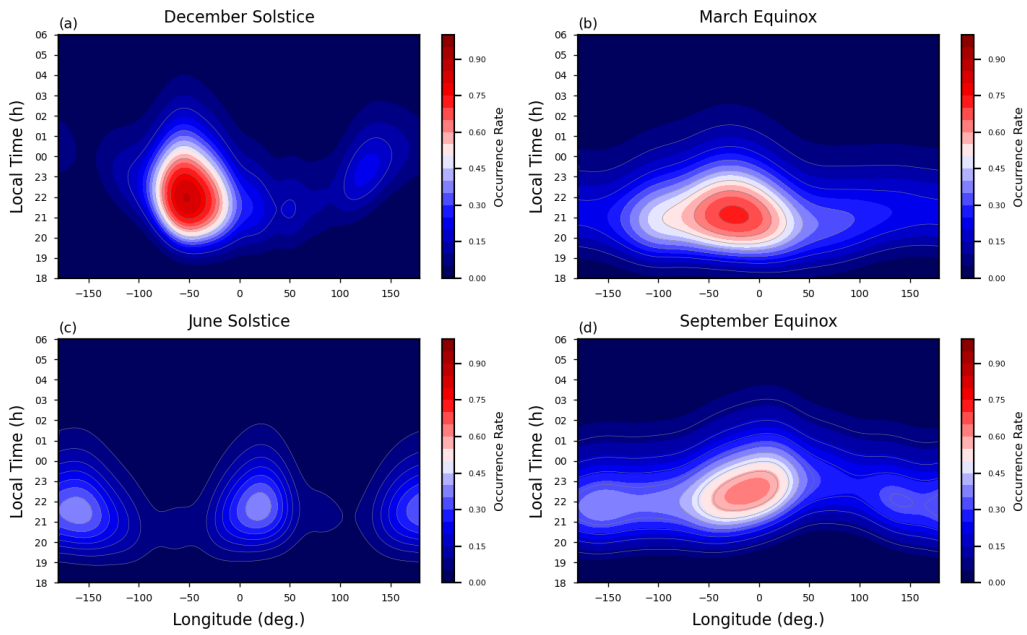


Figure 5. Occurrence probability of EPDs presented as a function of longitude and local time predicted by the IBP model at a constant F10.7 index of 150 s.f.u during (a) December, (b) March, (c) June, and (d) September.

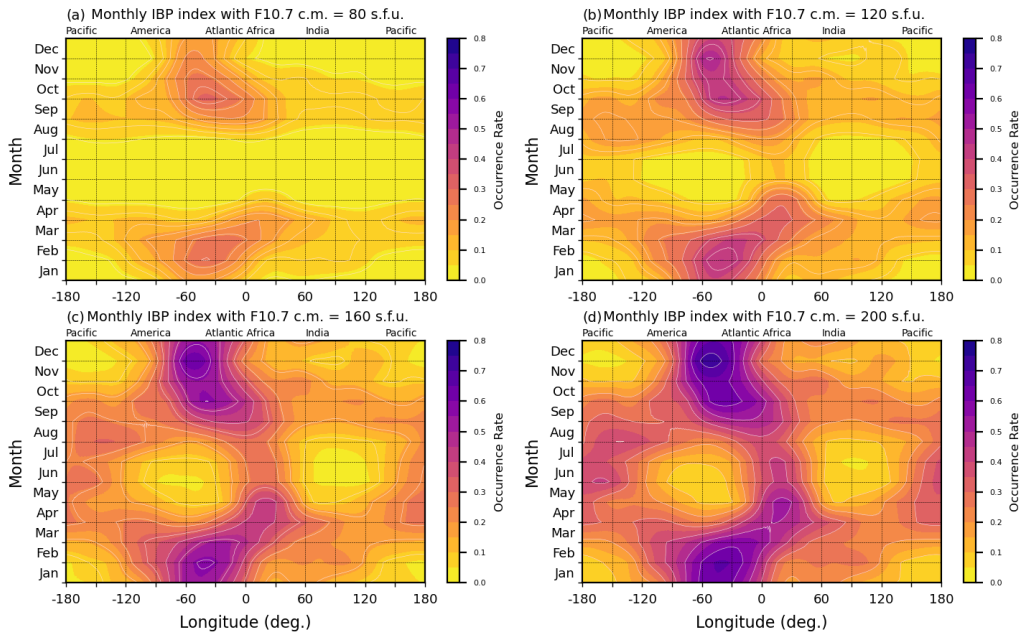


Figure 6. Occurrence probability of EPDs presented as a function of longitude and month predicted by the IBP model at F10.7 values of (a) 80 s.f.u, (b) 120 s.f.u, (c) 160 s.f.u and (d) 200 s.f.u.

361 rence rate from the IBP model, referred henceforth as monthly IBP index, is derived for
 362 a fixed value of F10.7 for all integer longitudes at a resolution of 5° at the middle of each
 363 month and averaged between 19 and 01 LT. We find that the IBP model reproduces the
 364 expected positive linear relationship between EPD occurrence rates and F10.7 index. The
 365 monthly IBP index generally retains negligible probabilities for F10.7 at 80 s.f.u except
 366 in the America-Atlantic-Africa sector during the equinoxes and solstice periods. How-
 367 ever, with increasing F10.7 levels, the monthly IBP indices begin to show significant prob-
 368 abilities as EPDs become more prevalent. Besides, with F10.7 at 120 s.f.u and above,
 369 the seasonal and longitudinal variations of the EPD occurrence rates are particularly well-
 370 characterized by the IBP model compared to its climatology (e.g., Gentile et al., 2006a)
 371 with monthly IBP index reaching highest rates around the equinoxes and winter solstice
 372 in the America-Atlantic-Africa region and lowest rates during November-February in the
 373 Pacific sector and during May-July in the America-Atlantic and Indian sectors. The re-
 374 sults from the IBP model showing a dependence on F10.7 levels compares well with the
 375 findings of Gentile et al. (2006b), which showed the climatology of EPD based on 15 years
 376 of plasma density measurements using the Defense Meteorological Satellite Program (DMSP)
 377 satellites.

378 5 Assessment of the IBP model

379 5.1 Overview of assessment methods

380 The performance of probabilistic predictions by models developed for space weather
 381 phenomena have been typically quantified in the literature using skill scores and rela-
 382 tive (receiver) operating characteristic (ROC) curves (e.g., Barnes et al., 2016; Murray
 383 et al., 2017; Nishizuka et al., 2020). A skill score is generally defined as the measure of
 384 accuracy of forecasts of interest relative to the accuracy of the forecasts produced by some
 385 reference procedure (Murphy, 1988). A generic skill score takes the following form,

$$Skill\ Score = \frac{A_{forecast} - A_{reference}}{A_{perfect} - A_{reference}} \quad (13)$$

386 where $A_{forecast}$ is the accuracy of the forecasting method under consideration, $A_{perfect}$
 387 is the accuracy of a perfect forecast and $A_{reference}$ is the accuracy of a reference method
 388 or the accuracy that is attainable by chance, which is usually chosen to be the clima-
 389 tology of the considered event. For probabilistic forecasts, a measure of accuracy is the
 390 mean square error (MSE), which can be used to calculate $A_{forecast}$ as shown in Barnes
 391 et al. (2016) in the following way,

$$A_{forecast} = MSE(p_f, o) = \langle (p_f - o)^2 \rangle \quad (14)$$

392 where p_f is the forecast probability from the considered method and o is the value
 393 for binary outcomes ($o = 0$ for non event, $o = 1$ for an event). The MSE for a per-
 394 fect forecast, $A_{perfect}$, is 0.

395 In this work, we use the Brier Skill Score (BSS) (Wilks, 1995) for evaluating the
 396 probability forecasting capability of the IBP model. BSS is calculated from the Brier score
 397 (BS) and climatological Brier score (BS_c) by using the following equation,

$$BSS = \frac{BS - BS_c}{0 - BS_c} \quad (15)$$

398 where $BS = MSE(p_f, o)$ and $BS_c = MSE(\langle o \rangle, o)$. BSS can be complemented
 399 by a reliability diagram, which compares the forecast probabilities with the observed fre-
 400 quency of the events.

401 The quality of the probability forecasts are also assessed by using the ROC curve,
 402 which relates the true positive rate (TPR) or the probability of detection (POD) against
 403 the corresponding false alarm rate (FAR) (e.g., Swets, 1973; Mason, 1982). TPR or POD
 404 and FAR can be easily understood in case of a binary categorical forecasting system us-
 405 ing a 2×2 contingency table (see Table 3).

Table 3. 2×2 contingency table for a binary, categorical forecasting system

Observation	Forecasts		
	Positive	Negative	Total
Event	True Positive (TP)	False Negative (FN)	TP+FN
Nonevent	False Positive (FP)	True Negative (TN)	FP+TN
Total	TP+FP	FN+TN	N=TP+FP+FN+TN

406 From the contingency table, POD and FAR are defined as follows (e.g., Mason, 1982)

$$POD = \frac{TP}{TP + FN} \quad \text{and} \quad FAR = \frac{FP}{FP + TN} \quad (16)$$

407 Probabilistic forecasts can be converted to binary, categorical forecasts by select-
 408 ing a probability threshold, P_{th} , such that any forecast probability over the threshold
 409 is considered to be a forecast for an event, and anything less is considered to be a fore-
 410 cast for a non-event. By varying this threshold value, contingency tables along with cor-
 411 responding POD and FAR can be determined for every P_{th} and based on these result-
 412 ing POD and FAR values, a ROC curve can be obtained. As POD and FAR are the axes
 413 of the ROC curve and they range between 0 and 1, the ROC curve for no-skill forecasts
 414 coincides with the 45° line from the origin passing through (0,0) and (1,1) with POD and
 415 FAR being equal. For a perfect forecast, the ROC curve connects the points (0,0), (0,1)
 416 and (1,1) with the values of POD and FAR being 1 and 0, respectively. The accuracy
 417 of binary, categorical forecasts can be determined using standard skill scores and can be
 418 summarized by the ROC Skill Score (ROCSS), also known as the Gini coefficient $G1$ (e.g.,
 419 Jolliffe & Stephenson, 2012) and by the Hanssen and Kuiper’s Discriminant (H&KSS),
 420 also known as the true skill statistic (TSS) or the Peirce skill score (e.g., Hanssen & Kuipers,
 421 1965; Murhy, 1993). $G1 = 2 \times A - 1.0$ where A is the area under the ROC curve, and
 422 $G1 = 1.0$ denotes a perfect score. H&KSS can be written as,

$$H\&KSS = POD - FAR \quad (17)$$

423 H&KSS takes into account the success due to random guessing and it ranges be-
 424 tween -1 and +1. A score of +1 indicates perfect agreement between predictions and ob-
 425 servations while a score of 0 or less indicate no-skill forecasting capability. As H&KSS
 426 can be sensitive to P_{th} , we also calculate the Gini coefficient to present a concise sum-
 427 mary of the assessment of the IBP model.

428 5.2 Model evaluation

429 We use one year of recent IBI index data from the Swarm A, B and C satellites be-
 430 tween July 2022 and June 2023 for the purpose of IBP model validation. During this pe-
 431 riod, the total number of orbits with and without EPD for each Swarm satellite are sum-
 432 marized in Table 4. For each orbit of the satellite, we first compute the EPD occurrence

433 probability from the IBP model for all longitude and local time that the satellite tra-
 434 verses. These probability outputs are then used to derive the maximum EPD occurrence
 435 probability for each satellite orbit. With different choices of probability threshold, P_{th} ,
 436 we predict using this derived maximum EPD occurrence probability whether each satel-
 437 lite orbit contains or not contains EPD. The contingency tables for binary, categorical
 438 forecasts of EPD is then created by varying P_{th} and compared with the observed IBI data
 439 set. We chose a threshold step of 0.02 resulting in covering the P_{th} levels between 0 and
 440 1. Thereafter, POD and FAR values are calculated for different contingency tables and
 441 ROC curves are generated for Swarm A, B and C satellites. These ROC curves are pre-
 442 sented in the upper panels of Figure 7 and are used to visualize H&KSS. When P_{th} is
 443 set to 1, no EPD detections are forecasted and hence TP=FP=0, which corresponds to
 444 the point (0,0) on the ROC curves. When P_{th} is set to 0, all detections are forecasted
 445 as EPD and hence FN=TN=0, which corresponds to the point (1,1) on the ROC curves.
 446 For Figures 7a-7c, we find that ROC curves stay well above the 45° no-skill forecast line
 447 shown here in dashed green color. The ROC curves also stay close to the FAR=0 while
 448 the POD rises, which suggests that the IBP model well forecasts EPD events. For Swarm
 449 satellites A, B and C, we find that H&KSS maximizes at at similar values, e.g., when
 450 P_{th} equals 0.22, 0.18 and 0.18, respectively, which is shown through dashed vertical black
 451 lines. H&KSS values reach 0.66, 0.73 and 0.65 for satellites A, B and C, respectively, which
 452 suggests that the forecasting capability of the IBP model is significantly better than a
 453 no-skill forecast. The Gini coefficient for Swarm A, B and C satellites are 0.80, 0.86 and
 454 0.80, respectively.

Table 4. Total number of orbits with and without EPD for each Swarm satellite between July 2022 and June 2023

Satellite	# of orbits		
	Total	with EPDs	without EPDs
A	3165	334	2831
B	3294	262	3032
C	3189	357	2832

455 In the lower panels of Figure 7, the BSS score and reliability plots that accompany
 456 it are presented for the three Swarm satellites. The BSS for Swarm A, B and C equal
 457 0.317, 0.320 and 0.316, respectively. The reliability plots are constructed by first select-
 458 ing probability intervals and then the frequency of observed events within each interval
 459 is estimated using the method described in Wheatland (2005). This observed frequency
 460 is then plotted against the predicted probability and the error bars are estimated based
 461 on the number of events that lie within each interval. On a reliability plot, perfect pre-
 462 diction corresponds to a 45° line when observed frequency equals the predicted proba-
 463 bility, which is plotted here using the dashed green lines in Figure 7d-f. Points lying above
 464 this line indicate underprediction while points located below this line imply overpredic-
 465 tion. We find that the IBP model underestimates the occurrence frequency of EPD when
 466 the predicted probability exceeds 0.7 for all three satellites. Below this predicted proba-
 467 bility value, the model slightly overestimates the occurrence frequency of EPD for all
 468 three satellites. We found, that the overestimation for low occurrence rates increases with
 469 the amount of data of very low solar flux. These times are usually free of EPD detec-
 470 tions in the topside F region. A reasonable results as shown in Figure 7, was found for
 471 a cutoff of $F10.7 \leq 80$ s.f.u.. In summary, the model slightly underestimates the EPD
 472 occurrence at occasions of high EPD probability and it slightly overestimates the EPD
 473 occurrence of low EPD probability. The performance of the IBP model based on the eval-
 474 uation metrics used here above is summarized in Table 5.

Table 5. IBP model performance based on the evaluation metrics for Swarm data between July 2022 and June 2023

Satellite	H&KSS (P_{th})	G1	BSS
A	0.66 (0.22)	0.80	0.317
B	0.73 (0.18)	0.86	0.320
C	0.65 (0.18)	0.80	0.316

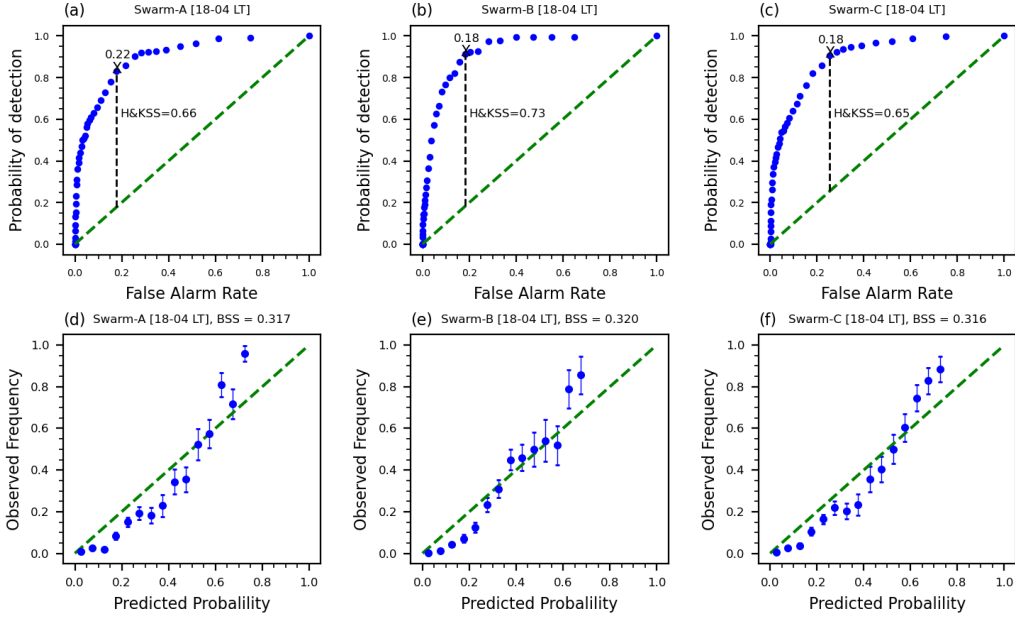


Figure 7. The top panels of the figure (a-c) show receiver operating characteristic (ROC) plots depicting the probability of detection as a function of the false alarm rate by varying the threshold above which an EPD is forecasted. In this case the maximum H&KSS occurs for $p = 0.22, 0.18, 0.18$ for Swarm A, B and C, respectively and is indicated by a dashed vertical line. The random classifier line of the ROC plots is denoted in dashed green colors. The bottom panels (d-f) show reliability plots in which the observed frequency of EPDs is plotted as a function of the forecast probability. Perfect reliability occurs when all points lie on the diagonal ($x=y$) line. The error bars are based on the sample sizes in each relevant bin.

6 Application of the IBP model

The IBP model estimates the occurrence probability of post-sunset equatorial plasma irregularities between 0 (EPDs not at all expected to occur) and 1 (EPDs are fully expected to occur) for a given longitude, local time, day of year, and solar flux value. The performance of the IBP model has been assessed as an estimate largely exceeding a non-skilled forecast in section 5. Thus, the model can be used to predict IBP occurrence with reasonable confidence. The model forward code is publicly made available, as being an official L2 product of the Swarm mission as given at https://swarmhandbook.earth.esa.int/catalogue/SW_IBP_CLI_2_. The forward model code itself and its documentations are available at Gitlab via <https://igit.iap-kborn.de/ibp/ibp-model>. The model code is provided in Python and is also available as a Python package. The model

486 coefficients will be updated with time, when more Swarm observations will be available.
 487 A yearly update is anticipated. Updates will be declared in the Gitlab documentation.

488 Besides the consideration of the assessment results given in section 5, the user of
 489 the IBP model shall be aware of the following constraints. The IBP model

- 490 • estimates the EPD occurrence rate at altitudes between 350 and 500 km, and does
 491 not give information on EPDs which do not reach these altitudes.
- 492 • is not recommended to be applied for solar flux indices $F_{10.7} \leq 80$ s.f.u. and $F_{10.7} \geq 200$ s.f.u..
- 493 • does not predict EPD occurrence depending on latitude. It provides the EPD oc-
 494 currence for a user-defined longitude, but integrated over latitude.

495 7 Conclusions

496 In this study, we have presented the IBP model by explaining its derivation, its as-
 497 sessment, and giving recommendations for its application. The main findings of this study
 498 are summarized below:

- 499 • The IBP model is a statistical climatological model for predicting the occurrence
 500 probability of F region EPDs for a given local time, solar radio flux, day of year,
 501 and longitude.
- 502 • It fully captures the climatology and solar flux dependence of EPDs at altitudes
 503 between 350 and 500 km. The model especially performs well in the American/Atlantic
 504 sector during December solstice and increased solar activity conditions, which is
 505 encouraging as this region and this season is a hotspot for EPDs.
- 506 • Based on one year of recent Swarm magnetic data, which constitutes as partly non-
 507 trained data set for the assessment, the IBP model has been evaluated and var-
 508 ious evaluation metrics have been presented. The IBP model shows improved pre-
 509 diction capability compared to climatological forecasts with moderate skill scores.
 510 With the addition of more recent Swarm data, e.g., by updating the model pa-
 511 rameters, it is expected that the skill scores and accuracy of the IBP model en-
 512 hances further.
- 513 • The IBP model is publicly made available at [https://igit.iap-kborn.de/ibp/
 514 ibp-model](https://igit.iap-kborn.de/ibp/ibp-model).

515 8 Open Research

516 The CHAMP magnetic data set used in this paper (Rother & Michaelis, 2019) can
 517 be freely downloaded using the following ftp link, [ftp://anonymous@isdcftp.gfz-potsdam
 518 .de/champ/](ftp://anonymous@isdcftp.gfz-potsdam.de/champ/). How to access the data and data citations can be found under [https://
 519 isdc.gfz-potsdam.de/champ-isdc/access-to-the-champ-data/](https://isdc.gfz-potsdam.de/champ-isdc/access-to-the-champ-data/). The Swarm data
 520 set is publicly available from the European Space Agency website using the following web-
 521 site link <https://earth.esa.int/eogateway/missions/swarm/data>. The IBP model
 522 is publicly available with the Gitlab link <https://igit.iap-kborn.de/ibp/ibp-model>.
 523 The F10.7 index is accessible at [https://lasp.colorado.edu/lisird/data/noaa_radio
 524 _flux](https://lasp.colorado.edu/lisird/data/noaa_radio_flux). The Hp30 index (Matzka et al., 2022) is provided at [https://kp.gfz-potsdam
 525 .de/en/hp30-hp60](https://kp.gfz-potsdam.de/en/hp30-hp60). All data sets and software are freely available from the stated links
 526 without the need for user registration. The CHAMP magnetic data set and the Hp30
 527 index are published under licence CC BY 4.0.

528 Acknowledgments

529 This work has been partly supported by Swarm DISC activities funded by ESA under
 530 contract no. 4000109587/13/I-NB.

531 **Appendix A Derivation of Equation 2**

$$\begin{aligned}
P[X(t) = 1] &= 1 - P[X(t) = 0] \\
&= 1 - P \left[\left\{ \sum_{i=1}^{N_\lambda} \mathbb{1}(T_0^{(i)} < t) \cdot \mathbb{1}(T_0^{(i)} + L^{(i)} > t) \right\} = 0 \right] \\
&= 1 - \sum_{i=1}^{\infty} e^{-\lambda} \frac{\lambda^k}{k!} P \left[\mathbb{1}(T_0^{(1)} < t) \cdot \mathbb{1}(T_0^{(1)} + L^{(1)} > t) = 0 \right]^i \\
&= 1 - \sum_{i=1}^{\infty} e^{-\lambda} \frac{\lambda^k}{k!} (1 - P \left[\mathbb{1}(T_0^{(1)} < t) \cdot \mathbb{1}(T_0^{(1)} + L^{(1)} > t) = 1 \right])^i \\
&= 1 - \sum_{i=1}^{\infty} e^{-\lambda} \frac{\lambda^k}{k!} (P \left[T_0^{(1)} > t \right] + P \left[T_0^{(1)} + L^{(1)} < t \right])^i \\
&= 1 - e^{-\lambda} \cdot e^{\lambda \cdot (P \left[T_0^{(1)} > t \right] + P \left[T_0^{(1)} + L^{(1)} < t \right])} \tag{A1} \\
&= 1 - e^{\lambda \cdot (P \left[T_0^{(1)} > t \right] + P \left[T_0^{(1)} + L^{(1)} < t \right] - 1)} \\
&= 1 - e^{\lambda \cdot (-P \left[T_0^{(1)} < t \right] + P \left[T_0^{(1)} + L^{(1)} < t \right])} \\
&= 1 - e^{\lambda \cdot (-\int_{-\infty}^t \frac{1}{\sqrt{2\pi}\sigma} e^{\frac{-(x-\mu)^2}{2\sigma^2}} dx + \int_{-\infty}^t \frac{1}{\sqrt{2\pi}\sigma} e^{\frac{-(x-\mu)^2}{2\sigma^2}} P \left[L^1 < t-x \right] dx)} \\
&= 1 - e^{\lambda \cdot (-\int_{-\infty}^t \frac{1}{\sqrt{2\pi}\sigma} e^{\frac{-(x-\mu)^2}{2\sigma^2}} dx + \int_{-\infty}^t \frac{1}{\sqrt{2\pi}\sigma} e^{\frac{-(x-\mu)^2}{2\sigma^2} (1 - e^{-\gamma \cdot (t-x)})} dx)} \\
&= 1 - e^{\lambda \cdot \left(\int_{-\infty}^t \frac{1}{\sqrt{2\pi}\sigma} e^{\frac{-(x-\mu)^2}{2\sigma^2}} (-e^{-\gamma(t-x)}) dx \right)} \\
&= 1 - e^{\lambda \cdot I(t, \gamma, \mu, \sigma)}
\end{aligned}$$

532 **References**

- 533 Aa, E., Zhang, S.-R., Coster, A. J., Erickson, P. J., & Rideout, W. (2023). Multi-
534 instrumental analysis of the day-to-day variability of equatorial plasma bubbles.
535 *Frontiers in Astronomy and Space Sciences*, 10. doi: <https://doi.org/10.3389/fspas.2023.1167245>
536
- 537 Aa, E., Zou, S., & Liu, S. (2020). Statistical Analysis of Equatorial Plasma Irreg-
538 ularities Retrieved From Swarm 2013–2019 Observations. *Journal of Geophysical*
539 *Research: Space Physics*, 125(4), e2019JA027022. doi: <https://doi.org/10.1029/2019JA027022>
540
- 541 Abdu, M. A. (2019). Day-to-day and short-term variabilities in the equatorial
542 plasma bubble/spread F irregularity seeding and development. *Progress in Earth*
543 *and Planetary Science*, 6(1), 11. doi: <https://doi.org/10.1186/s40645-019-0258-1>
544
- 545 Abdu, M. A., de Medeiros, R. T., Bittencourt, J. A., & Batista, I. S. (1983). Ver-
546 tical ionization drift velocities and range type spread F in the evening equatorial
547 ionosphere. *Journal of Geophysical Research: Space Physics*, 88(A1), 399-402. doi:
<https://doi.org/10.1029/JA088iA01p00399>
- 548 Balsley, B. B., Haerendel, G., & Greenwald, R. A. (1972). Equatorial spread F:
549 Recent observations and a new interpretation. *Journal of Geophysical Research*
550 *(1896-1977)*, 77(28), 5625-5628. doi: <https://doi.org/10.1029/JA077i028p05625>
- 551 Barnes, G., Leka, K. D., Schrijver, C. J., Colak, T., Qahwaji, R., Ashamari, O. W.,
552 ... Wagner, E. L. (2016). A comparison of flare forecasting methods. I. Results
553 from the “All-Clear” workshop. *The Astrophysical Journal*, 829(2), 89. doi:
554 <https://10.3847/0004-637X/829/2/89>
- 555 Basu, S., Basu, S., Huba, J., Krall, J., McDonald, S. E., Makela, J. J., ... Groves,
556 K. (2009). Day-to-day variability of the equatorial ionization anomaly and

- 557 scintillations at dusk observed by GUVI and modeling by SAMI3. *Journal of*
 558 *Geophysical Research: Space Physics*, 114(A4). doi: [https://doi.org/10.1029/](https://doi.org/10.1029/2008JA013899)
 559 2008JA013899
- 560 Burke, W. J., Gentile, L. C., Huang, C. Y., Valladares, C. E., & Su, S. Y. (2004).
 561 Longitudinal variability of equatorial plasma bubbles observed by DMSP and
 562 ROCSAT-1. *Journal of Geophysical Research: Space Physics*, 109(A12). doi:
 563 <https://doi.org/10.1029/2004JA010583>
- 564 Carter, B. A., Yizengaw, E., Retterer, J. M., Francis, M., Terkildsen, M., Marshall,
 565 R., ... Zhang, K. (2014). An analysis of the quiet time day-to-day variability
 566 in the formation of postsunset equatorial plasma bubbles in the Southeast Asian
 567 region. *Journal of Geophysical Research: Space Physics*, 119(4), 3206-3223. doi:
 568 <https://doi.org/10.1002/2013JA019570>
- 569 Chou, M.-Y., Pedatella, N. M., Wu, Q., Huba, J. D., Lin, C. C. H., Schreiner,
 570 W. S., ... Yue, J. (2020). Observation and Simulation of the Development
 571 of Equatorial Plasma Bubbles: Post-Sunset Rise or Upwelling Growth? *Jour-*
 572 *nal of Geophysical Research: Space Physics*, 125(12), e2020JA028544. doi:
 573 <https://doi.org/10.1029/2020JA028544>
- 574 Clemesha, B., & Wright, R. (1966). Spread-F and its Effects upon Radio Wave
 575 Propagation and Communications. *P. Newman, Téchnivision. England*, 3.
- 576 Dabas, R. S., Singh, L., Lakshmi, D. R., Subramanyam, P., Chopra, P., & Garg,
 577 S. C. (2003). Evolution and dynamics of equatorial plasma bubbles: Relation-
 578 ships to ExB drift, postsunset total electron content enhancements, and equa-
 579 torial electrojet strength. *Radio Science*, 38(4). doi: [https://doi.org/10.1029/](https://doi.org/10.1029/2001RS002586)
 580 2001RS002586
- 581 Das, S. K., Patra, A. K., & Niranjana, K. (2021). On the Assessment of Day-To-Day
 582 Occurrence of Equatorial Plasma Bubble. *Journal of Geophysical Research: Space*
 583 *Physics*, 126(5), e2021JA029129. doi: <https://doi.org/10.1029/2021JA029129>
- 584 Fagundes, P. R., Sahai, Y., Batista, I. S., Abdu, M. A., Bittencourt, J. A., & Taka-
 585 hashi, H. (1999). Observations of day-to-day variability in precursor signatures to
 586 equatorial F-region plasma depletions. *Annales Geophysicae*, 17(8), 1053-1063.
 587 doi: <https://10.1007/s00585-999-1053-x>
- 588 Farley, D. T., Balsey, B. B., Woodman, R. F., & McClure, J. P. (1970). Equa-
 589 torial spread F: Implications of VHF radar observations. *Journal of Geophys-*
 590 *ical Research (1896-1977)*, 75(34), 7199-7216. doi: [https://doi.org/10.1029/](https://doi.org/10.1029/JA075i034p07199)
 591 JA075i034p07199
- 592 Fejer, B. G., Scherliess, L., & de Paula, E. R. (1999). Effects of the vertical plasma
 593 drift velocity on the generation and evolution of equatorial spread F. *Journal of*
 594 *Geophysical Research: Space Physics*, 104(A9), 19859-19869. doi: [https://doi.org/](https://doi.org/10.1029/1999JA900271)
 595 10.1029/1999JA900271
- 596 Friis-Christensen, E., Lühr, H., & Hulot, G. (2006). Swarm: A constellation to study
 597 the Earth's magnetic field. *Earth, Planets and Space*, 58(4), 351-358. doi: [https://](https://doi.org/10.1186/BF03351933)
 598 doi.org/10.1186/BF03351933
- 599 Fukao, S., Yokoyama, T., Tayama, T., Yamamoto, M., Maruyama, T., & Saito, S.
 600 (2006). Eastward traverse of equatorial plasma plumes observed with the Equa-
 601 torial Atmosphere Radar in Indonesia. *Annales Geophysicae*, 24(5), 1411-1418.
 602 Retrieved from <https://angeo.copernicus.org/articles/24/1411/2006/> doi:
 603 10.5194/angeo-24-1411-2006
- 604 Gentile, L. C., Burke, W. J., & Rich, F. J. (2006a). A climatology of equatorial
 605 plasma bubbles from DMSP 1989-2004. *Radio Science*, 41(5). doi: [https://doi](https://doi.org/10.1029/2005RS003340)
 606 [.org/10.1029/2005RS003340](https://doi.org/10.1029/2005RS003340)
- 607 Gentile, L. C., Burke, W. J., & Rich, F. J. (2006b). A global climatology for equa-
 608 torial plasma bubbles in the topside ionosphere. *Annales Geophysicae*, 24(1), 163-
 609 172. doi: <https://doi.org/10.5194/angeo-24-163-2006>
- 610 Gentile, L. C., Burke, W. J., Roddy, P. A., Retterer, J. M., & Tsunoda, R. T.

- 611 (2011). Climatology of plasma density depletions observed by DMSP in the
 612 dawn sector. *Journal of Geophysical Research: Space Physics*, 116(A3). doi:
 613 <https://doi.org/10.1029/2010JA016176>
- 614 Haerendel, G. (1973). Theory of equatorial spread F. *Space Plasma Physics of Near-*
 615 *Earth Environment*, MPI for Extraterrestrial Physics, Max Planck Society.
- 616 Hanssen, A., & Kuipers, W. (1965). *On the relationship between the frequency of*
 617 *rain and various meteorological parameters. (With reference to the problem of*
 618 *objective forecasting)*. Koninklijk Nederlands Meteorologisch Instituut.
- 619 Huang, C.-S., de La Beaujardiere, O., Roddy, P. A., Hunton, D. E., Liu, J. Y., &
 620 Chen, S. P. (2014). Occurrence probability and amplitude of equatorial iono-
 621 spheric irregularities associated with plasma bubbles during low and moderate
 622 solar activities (2008–2012). *Journal of Geophysical Research: Space Physics*,
 623 119(2), 1186-1199. doi: <https://doi.org/10.1002/2013JA019212>
- 624 Huang, C.-S., & Hairston, M. R. (2015). The postsunset vertical plasma drift and its
 625 effects on the generation of equatorial plasma bubbles observed by the C/NOFS
 626 satellite. *Journal of Geophysical Research: Space Physics*, 120(3), 2263-2275. doi:
 627 <https://doi.org/10.1002/2014JA020735>
- 628 Hysell, D., & Burcham, J. (2002). Long term studies of equatorial spread F us-
 629 ing the JULIA radar at Jicamarca. *Journal of Atmospheric and Solar-Terrestrial*
 630 *Physics*, 64(12), 1531-1543. (Equatorial Aeronomy) doi: [https://doi.org/10.1016/S1364-6826\(02\)00091-3](https://doi.org/10.1016/S1364-6826(02)00091-3)
- 632 Hysell, D. L., Fang, T. W., & Fuller-Rowell, T. J. (2022). Modeling equato-
 633 rial f-region ionospheric instability using a regional ionospheric irregularity
 634 model and wam-ipe. *Journal of Geophysical Research: Space Physics*, 127(9),
 635 e2022JA030513. doi: <https://doi.org/10.1029/2022JA030513>
- 636 Hysell, D. L., Rojas, E., Goldberg, H., Milla, M. A., Kuyeng, K., Valdez, A., ...
 637 Bourne, H. (2021). Mapping irregularities in the postsunset equatorial ionosphere
 638 with an expanded network of hf beacons. *Journal of Geophysical Research: Space*
 639 *Physics*, 126(7), e2021JA029229. doi: <https://doi.org/10.1029/2021JA029229>
- 640 Hysell, D. L., & Seyler, C. E. (1998). A renormalization group approach to esti-
 641 mation of anomalous diffusion in the unstable equatorial F region. *Journal of Geo-*
 642 *physical Research: Space Physics*, 103(A11), 26731-26737. doi: [https://doi.org/10](https://doi.org/10.1029/98JA02616)
 643 [.1029/98JA02616](https://doi.org/10.1029/98JA02616)
- 644 Jolliffe, I. T., & Stephenson, D. B. (2012). *Forecast verification: a practitioner's*
 645 *guide in atmospheric science*. John Wiley & Sons.
- 646 Kelley, M. C. (2009). *The earth's ionosphere: Plasma physics and electrodynamics*.
 647 Academic press.
- 648 Kil, H., & Heelis, R. A. (1998a). Equatorial density irregularity structures at in-
 649 termediate scales and their temporal evolution. *Journal of Geophysical Research:*
 650 *Space Physics*, 103(A3), 3969-3981. doi: <https://doi.org/10.1029/97JA03344>
- 651 Kil, H., & Heelis, R. A. (1998b). Global distribution of density irregularities in the
 652 equatorial ionosphere. *Journal of Geophysical Research: Space Physics*, 103(A1),
 653 407-417. doi: <https://doi.org/10.1029/97JA02698>
- 654 Kil, H., Heelis, R. A., Paxton, L. J., & Oh, S.-J. (2009). Formation of a plasma de-
 655 pletion shell in the equatorial ionosphere. *Journal of Geophysical Research: Space*
 656 *Physics*, 114(A11). doi: <https://doi.org/10.1029/2009JA014369>
- 657 Knudsen, D. J., Burchill, J. K., Buchert, S. C., Eriksson, A. I., Gill, R., Wahlund,
 658 J.-E., ... Moffat, B. (2017). Thermal ion imagers and Langmuir probes in the
 659 Swarm electric field instruments. *Journal of Geophysical Research: Space Physics*,
 660 122(2), 2655-2673. doi: <https://doi.org/10.1002/2016JA022571>
- 661 Kudeki, E., & Bhattacharyya, S. (1999). Postsunset vortex in equatorial F-region
 662 plasma drifts and implications for bottomside spread-F. *Journal of Geophysical*
 663 *Research: Space Physics*, 104(A12), 28163-28170. doi: [https://doi.org/10.1029/](https://doi.org/10.1029/1998JA900111)
 664 [1998JA900111](https://doi.org/10.1029/1998JA900111)

- 665 Li, G., Ning, B., Otsuka, Y., Abdu, M. A., Abadi, P., Liu, Z., . . . Wan, W. (2021,
666 Jan 01). Challenges to Equatorial Plasma Bubble and Ionospheric Scintillation
667 Short-Term Forecasting and Future Aspects in East and Southeast Asia. *Surveys*
668 *in Geophysics*, *42*(1), 201-238. doi: <https://doi.org/10.1007/s10712-020-09613-5>
- 669 Lühr, H., Maus, S., Rother, M., & Cooke, D. (2002). First in-situ observation of
670 night-time F region currents with the CHAMP satellite. *Geophysical Research Let-*
671 *ters*, *29*(10), 127-1-127-4. doi: <https://doi.org/10.1029/2001GL013845>
- 672 Lühr, H., Rother, M., Maus, S., Mai, W., & Cooke, D. (2003). The diamag-
673 netic effect of the equatorial appleton anomaly: Its characteristics and impact
674 on geomagnetic field modeling. *Geophysical Research Letters*, *30*(17). doi:
675 <https://doi.org/10.1029/2003GL017407>
- 676 Lühr, H., Xiong, C., Park, J., & Rauberg, J. (2014). Systematic study of
677 intermediate-scale structures of equatorial plasma irregularities in the ionosphere
678 based on CHAMP observations. *Frontiers in Physics*, *2*. doi: <https://doi.org/10.3389/fphy.2014.00015>
- 680 Macho, E. P., Correia, E., Spogli, L., & Tadeu de Assis Honorato Muella, M. (2022).
681 Climatology of ionospheric amplitude scintillation on gnss signals at south amer-
682 ican sector during solar cycle 24. *Journal of Atmospheric and Solar-Terrestrial*
683 *Physics*, *231*, 105872. doi: <https://doi.org/10.1016/j.jastp.2022.105872>
- 684 Manju, G., & Aswathy, R. P. (2020). Ionospheric Planetary Wave Activity and Its
685 Role in Equatorial Spread F Day-to-Day Variability. *Journal of Geophysical Re-*
686 *search: Space Physics*, *125*(9), e2020JA027960. (e2020JA027960 2020JA027960)
687 doi: <https://doi.org/10.1029/2020JA027960>
- 688 Martinis, C., Daniell, R., Eastes, R., Norrell, J., Smith, J., Klenzing, J., . . . Burns,
689 A. (2021). Longitudinal Variation of Postsunset Plasma Depletions From
690 the Global-Scale Observations of the Limb and Disk (GOLD) Mission. *Jour-*
691 *nal of Geophysical Research: Space Physics*, *126*(2), e2020JA028510. doi:
692 <https://doi.org/10.1029/2020JA028510>
- 693 Martinis, C., & Mendillo, M. (2007). Equatorial spread F-related airglow depletions
694 at Arecibo and conjugate observations. *Journal of Geophysical Research: Space*
695 *Physics*, *112*(A10). doi: <https://doi.org/10.1029/2007JA012403>
- 696 Mason, I. (1982). A Model for Assessment of Weather Forecasts. *Australian Meteo-*
697 *rological Magazine*, *30*, 291-303.
- 698 Matzka, J., Bronkalla, O., Kervalishvili, G., Rauberg, J., Stolle, C., & Yamazaki,
699 Y. (2022). *Geomagnetic Hpo index. V. 2.0*. [Dataset]. GFZ Data Services. doi:
700 <https://doi.org/10.5880/Hpo.0002>
- 701 Murhy, A. H. (1993). What Is a Good Forecast? An Essay on the Nature of Good-
702 ness in Weather Forecasting. *Weather and Forecasting*, *8*(2), 281-293. doi:
703 [https://doi.org/10.1175/1520-0434\(1993\)008<0281:WIAGFA>2.0.CO;2](https://doi.org/10.1175/1520-0434(1993)008<0281:WIAGFA>2.0.CO;2)
- 704 Murphy, J. M. (1988). The impact of ensemble forecasts on predictability. *Quar-*
705 *terly Journal of the Royal Meteorological Society*, *114*(480), 463-493. doi: [https://](https://doi.org/10.1002/qj.49711448010)
706 doi.org/10.1002/qj.49711448010
- 707 Murray, S. A., Bingham, S., Sharpe, M., & Jackson, D. R. (2017). Flare forecasting
708 at the Met Office Space Weather Operations Centre. *Space Weather*, *15*(4), 577-
709 588. doi: <https://doi.org/10.1002/2016SW001579>
- 710 Nishizuka, N., Kubo, Y., Sugiura, K., Den, M., & Ishii, M. (2020). Reliable Prob-
711 ability Forecast of Solar Flares: Deep Flare Net-Reliable (DeFN-R). *The Astro-*
712 *physical Journal*, *899*(2), 150. doi: [10.3847/1538-4357/aba2f2](https://doi.org/10.3847/1538-4357/aba2f2)
- 713 Olsen, N., Friis-Christensen, E., Floberghagen, R., Alken, P., Beggan, C. D., Chul-
714 liat, A., . . . Visser, P. N. (2013). The Swarm Satellite Constellation Application
715 and Research Facility (SCARF) and Swarm data products. *Earth, Planets and*
716 *Space*, *65*(11), 1189-1200. doi: <https://doi.org/10.5047/eps.2013.07.001>
- 717 Ossakow, S. L. (1981). Spread-F theories-A review. *Journal of Atmospheric and Ter-*
718 *restrial Physics*, *43*(5), 437-452. doi: [https://doi.org/10.1016/0021-9169\(81\)90107](https://doi.org/10.1016/0021-9169(81)90107)

719

-0

720

Park, J., Noja, M., Stolle, C., & Lühr, H. (2013). The Ionospheric Bubble Index deduced from magnetic field and plasma observations onboard Swarm. *Earth, Planets and Space*, *65*(11), 1333-1344. doi: <https://doi.org/10.5047/eps.2013.08.005>

721

722

723

Patra, A. K., & Das, S. K. (2023). On the Upwelling of the F Layer Base and Prediction of Equatorial Plasma Bubble. *Geophysical Research Letters*, *50*(7), e2023GL102803. doi: <https://doi.org/10.1029/2023GL102803>

724

725

726

Rajesh, P. K., Lin, C. C. H., Chen, C. H., Chen, W. H., Lin, J. T., Chou, M. Y., ... You, C. F. (2017). Global equatorial plasma bubble growth rates using ionosphere data assimilation. *Journal of Geophysical Research: Space Physics*, *122*(3), 3777-3787. doi: <https://doi.org/10.1002/2017JA023968>

727

728

729

730

Reddy, S. A., Forsyth, C., Aruliah, A., Smith, A., Bortnik, J., Aa, E., ... Lewis, G. (2023). Predicting Swarm Equatorial Plasma Bubbles via Machine Learning and Shapley Values. *Journal of Geophysical Research: Space Physics*, *128*(6), e2022JA031183. doi: <https://doi.org/10.1029/2022JA031183>

731

732

733

734

Reigber, C., Lühr, H., & Schwintzer, P. (2002). CHAMP mission status. *Advances in Space Research*, *30*(2), 129-134. doi: [https://doi.org/10.1016/S0273-1177\(02\)00276-4](https://doi.org/10.1016/S0273-1177(02)00276-4)

735

736

737

Retterer, J. M., & Roddy, P. (2014). Faith in a seed: on the origins of equatorial plasma bubbles. *Annales Geophysicae*, *32*(5), 485-498. doi: <https://doi.org/10.5194/angeo-32-485-2014>

738

739

740

Rodríguez-Zuluaga, J., Stolle, C., Yamazaki, Y., Lühr, H., Park, J., Scherliess, L., & Chau, J. L. (2019). On the Balance Between Plasma and Magnetic Pressure Across Equatorial Plasma Depletions. *Journal of Geophysical Research: Space Physics*, *124*(7), 5936-5944. doi: <https://doi.org/10.1029/2019JA026700>

741

742

743

744

Rother, M., & Michaelis, I. (2019). *CH-ME-3-MAG - CHAMP 1 Hz Combined Magnetic Field Time Series (Level 3)* [Dataset]. GFZ Data Services. doi: <https://doi.org/10.5880/GFZ.2.3.2019.004>

745

746

747

Sahai, Y., Aarons, J., Mendillo, M., Baumgardner, J., Bittencourt, J., & Takahashi, H. (1994). OI 630 nm imaging observations of equatorial plasma depletions at 16° S dip latitude. *Journal of Atmospheric and Terrestrial Physics*, *56*(11), 1461-1475. doi: [https://doi.org/10.1016/0021-9169\(94\)90113-9](https://doi.org/10.1016/0021-9169(94)90113-9)

748

749

750

751

Sahai, Y., Fagundes, P., & Bittencourt, J. (2000). Transequatorial F-region ionospheric plasma bubbles: solar cycle effects. *Journal of Atmospheric and Solar-Terrestrial Physics*, *62*(15), 1377-1383. doi: [https://doi.org/10.1016/S1364-6826\(00\)00179-6](https://doi.org/10.1016/S1364-6826(00)00179-6)

752

753

754

755

Saito, S., & Maruyama, T. (2006). Ionospheric height variations observed by ionosondes along magnetic meridian and plasma bubble onsets. *Annales Geophysicae*, *24*(11), 2991-2996. doi: <https://doi.org/10.5194/angeo-24-2991-2006>

756

757

758

Saito, S., & Maruyama, T. (2007). Large-scale longitudinal variation in ionospheric height and equatorial spread F occurrences observed by ionosondes. *Geophysical Research Letters*, *34*(16). doi: <https://doi.org/10.1029/2007GL030618>

759

760

761

Sheather, S. J., & Jones, M. C. (1991). A Reliable Data-Based Bandwidth Selection Method for Kernel Density Estimation. *Journal of the Royal Statistical Society: Series B (Methodological)*, *53*(3), 683-690. doi: <https://doi.org/10.1111/j.2517-6161.1991.tb01857.x>

762

763

764

765

Shinagawa, H., Jin, H., Miyoshi, Y., Fujiwara, H., Yokoyama, T., & Otsuka, Y. (2018). Daily and seasonal variations in the linear growth rate of the Rayleigh-Taylor instability in the ionosphere obtained with GAIA. *Progress in Earth and Planetary Science*, *5*(1), 16. doi: <https://doi.org/10.1186/s40645-018-0175-8>

766

767

768

769

Singh, S., Johnson, F. S., & Power, R. A. (1997). Gravity wave seeding of equatorial plasma bubbles. *Journal of Geophysical Research: Space Physics*, *102*(A4), 7399-7410. doi: <https://doi.org/10.1029/96JA03998>

770

771

772

Stolle, C., Lühr, H., & Fejer, B. G. (2008). Relation between the occurrence

- 773 rate of ESF and the equatorial vertical plasma drift velocity at sunset derived
 774 from global observations. *Annales Geophysicae*, 26(12), 3979–3988. doi:
 775 <https://doi.org/10.5194/angeo-26-3979-2008>
- 776 Stolle, C., Lühr, H., Rother, M., & Balasis, G. (2006). Magnetic signatures of equa-
 777 torial spread F as observed by the CHAMP satellite. *Journal of Geophysical Re-*
 778 *search: Space Physics*, 111(A2). doi: <https://doi.org/10.1029/2005JA011184>
- 779 Su, S.-Y., Chao, C. K., & Liu, C. H. (2008). On monthly/seasonal/longitudinal vari-
 780 ations of equatorial irregularity occurrences and their relationship with the post-
 781 sunset vertical drift velocities. *Journal of Geophysical Research: Space Physics*,
 782 113(A5). doi: <https://doi.org/10.1029/2007JA012809>
- 783 Su, S.-Y., Yeh, H. C., & Heelis, R. A. (2001). ROCSAT 1 ionospheric plasma and
 784 electrodynamic instrument observations of equatorial spread F: An early transi-
 785 tional scale result. *Journal of Geophysical Research: Space Physics*, 106(A12),
 786 29153–29159. doi: <https://doi.org/10.1029/2001JA900109>
- 787 Sultan, P. J. (1996). Linear theory and modeling of the Rayleigh-Taylor instability
 788 leading to the occurrence of equatorial spread F. *Journal of Geophysical Research:*
 789 *Space Physics*, 101(A12), 26875–26891. doi: <https://doi.org/10.1029/96JA00682>
- 790 Swets, J. A. (1973). The Relative Operating Characteristic in Psychology: A tech-
 791 nique for isolating effects of response bias finds wide use in the study of perception
 792 and cognition. *Science*, 182(4116), 990–1000.
- 793 Tapping, K. F. (2013). The 10.7cm solar radio flux (f10.7). *Space Weather*, 11(7),
 794 394–406. doi: <https://doi.org/10.1002/swe.20064>
- 795 Tsunoda, R. T. (2005). On the enigma of day-to-day variability in equatorial
 796 spread F. *Geophysical Research Letters*, 32(8). doi: <https://doi.org/10.1029/2005GL022512>
- 797
 798 Tsunoda, R. T., Bubenik, D. M., Thampi, S. V., & Yamamoto, M. (2010). On
 799 large-scale wave structure and equatorial spread F without a post-sunset rise of
 800 the F layer. *Geophysical Research Letters*, 37(7). doi: <https://doi.org/10.1029/2009GL042357>
- 801
 802 Tsunoda, R. T., Saito, S., & Nguyen, T. T. (2018). Post-sunset rise of equatorial
 803 F layer—or upwelling growth? *Progress in Earth and Planetary Science*, 5(1), 22.
 804 doi: <https://doi.org/10.1186/s40645-018-0179-4>
- 805 Tsunoda, R. T., & White, B. R. (1981). On the generation and growth of equa-
 806 torial backscatter plumes 1. Wave structure in the bottomside F layer. *Journal of*
 807 *Geophysical Research: Space Physics*, 86(A5), 3610–3616. doi: [https://doi.org/10](https://doi.org/10.1029/JA086iA05p03610)
 808 [.1029/JA086iA05p03610](https://doi.org/10.1029/JA086iA05p03610)
- 809 Wheatland, M. S. (2005). A statistical solar flare forecast method. *Space Weather*,
 810 3(7). doi: <https://doi.org/10.1029/2004SW000131>
- 811 Wilks, D. (1995). *Forecast verification. Statistical methods in the atmospheric sci-*
 812 *ences*. Academic Press New York, NY, USA.
- 813 Woodman, R. F., & La Hoz, C. (1976). Radar observations of F region equatorial ir-
 814 regularities. *Journal of Geophysical Research (1896-1977)*, 81(31), 5447–5466. doi:
 815 <https://doi.org/10.1029/JA081i031p05447>
- 816 Xiong, C., Park, J., Lühr, H., Stolle, C., & Ma, S. Y. (2010). Comparing
 817 plasma bubble occurrence rates at CHAMP and GRACE altitudes during
 818 high and low solar activity. *Annales Geophysicae*, 28(9), 1647–1658. Re-
 819 trieved from <https://angeo.copernicus.org/articles/28/1647/2010/> doi:
 820 [10.5194/angeo-28-1647-2010](https://doi.org/10.5194/angeo-28-1647-2010)
- 821 Xiong, C., Stolle, C., & Lühr, H. (2016). The Swarm satellite loss of GPS signal
 822 and its relation to ionospheric plasma irregularities. *Space Weather*, 14(8), 563-
 823 577. Retrieved from [https://agupubs.onlinelibrary.wiley.com/doi/abs/10](https://agupubs.onlinelibrary.wiley.com/doi/abs/10.1002/2016SW001439)
 824 [.1002/2016SW001439](https://doi.org/10.1002/2016SW001439) doi: <https://doi.org/10.1002/2016SW001439>
- 825 Xiong, C., Xu, J.-S., Stolle, C., van den Ijssel, J., Yin, F., Kervalishvili, G. N., &
 826 Zangerl, F. (2020). On the Occurrence of GPS Signal Amplitude Degradation for

- 827 Receivers on Board LEO Satellites. *Space Weather*, 18(2), e2019SW002398. doi:
828 <https://doi.org/10.1029/2019SW002398>
- 829 Yamamoto, M., Otsuka, Y., Jin, H., & Miyoshi, Y. (2018). Relationship between
830 day-to-day variability of equatorial plasma bubble activity from GPS scintillation
831 and atmospheric properties from Ground-to-topside model of Atmosphere and
832 Ionosphere for Aeronomy (GAIA) assimilation. *Progress in Earth and Planetary
833 Science*, 5(1), 26. doi: <https://doi.org/10.1186/s40645-018-0184-7>
- 834 Yamazaki, Y., Matzka, J., Stolle, C., Kervalishvili, G., Rauberg, J., Bronkalla, O.,
835 ... Jackson, D. R. (2022). Geomagnetic Activity Index Hpo. *Geophysical Research
836 Letters*, 49(10), e2022GL098860. doi: <https://doi.org/10.1029/2022GL098860>
- 837 Zhan, W., Rodrigues, F. S., & Milla, M. A. (2018). On the Genesis of Postmidnight
838 Equatorial Spread F: Results for the American/Peruvian Sector. *Geophysical Re-
839 search Letters*, 45(15), 7354-7361. doi: <https://doi.org/10.1029/2018GL078822>